Icarus 361 (2021) 114368

Contents lists available at ScienceDirect

Icarus

journal homepage: www.elsevier.com/locate/icarus

Dynamic evolution of major element chemistry in protoplanetary disks and its implications for Earth-enstatite chondrite connection

Yoshinori Miyazaki [1,*], Jun Korenaga

Department of Earth and Planetary Sciences, Yale University, New Haven, CT 06511, USA

ARTICLE INFO

Keywords:
Protoplanetary disk
Chondrites
Major element fractionation

ABSTRACT

Chondrites are the likely building blocks of Earth, and identifying the group of chondrite that best represents Earth is a key to resolving the state of the early Earth. The origin of chondrites, however, remains controversial partly because of their puzzling major element compositions, some exhibiting depletion in Al, Ca, and Mg. Based on a new thermochemical evolution model of protoplanetary disks, we show that planetesimals with depletion patterns similar to ordinary and enstatite chondrites can originate at 1–2 AU outside where enstatite evaporates. Around the "evaporation front" of enstatite, the large inward flow of refractory minerals, including forsterite, takes place with a high pebble concentration, and the loss of those minerals results in depletion in Al, Ca, and Mg. The fractionation driven by the loss of forsterite would also create a complementary Mg-rich reservoir just inside the depleted region, creating two chemically distinct reservoirs adjacent to each other. The region around the evaporation front of enstatite has the highest dust concentration inside the snow line, and thus the streaming instability is most likely to be triggered therein. Planetesimals with two different major element compositions could naturally be created in the terrestrial region, which could evolve into parent bodies for Earth and chondrites. This can explain why Earth and enstatite chondrites share similar isotopic signatures but have different bulk compositions.

1. Introduction

Chondrites are a promising candidate for the building blocks of Earth, providing important constraints on the bulk chemistry, volatile inventory, and redox state of Earth's primitive mantle (McDonough and Sun 1995; Lyubetskaya and Korenaga, 2007; Dauphas 2017). There has been a long-standing debate over which chondrite group is the best representative of Earth, but no group perfectly matches the mantle in terms of both chemical and isotopic compositions (Jagoutz et al. 1979; Allègre et al.,1995; Javoy 1995). Among different chondrite groups, enstatite chondrites are isotopically the closest to Earth (Clayton and Mayeda 1984; Dauphas et al. 2004), whereas carbonaceous chondrites are the most similar in terms of the bulk composition (Wasson and Kallemeyn 1988; Halliday and Wood 2015). One of the difficulties in identifying the building blocks arises from our limited understanding of the mechanisms that are responsible for the major element compositions of chondrites. Ordinary and enstatite chondrites are depleted in refractory elements including Al, Ca, and Mg (Fig. 1), but such depletion is enigmatic from the perspective of the volatility trend (Lodders 2003; Albarède et al. 2014). The nebular gas dissipates as the protoplanetary disk cools down, so depletion is expected for volatile elements, not for refractory elements (Cassen 1996; Ciesla 2008; Li et al. 2020). Also, the enrichment of moderately volatile elements including Na, with respect to Al, Ca, and Mg, is observed in the EH class of enstatite chondrites (Fig. 1), making their origin even more puzzling (Wasson and Kallemeyn 1988).

The diverse compositions of chondrites have been explained by different proportions of their constituents. Chondrites contain four major components: Ca-Al-rich inclusion (CAI), chondrule, metallic Fe, and matrix. The loss of CAIs has been proposed to explain the depletion of refractory elements including Al and Ca. This is corroborated by astrophysical models as CAIs are likely lost to the Sun within the timescale of nebular evolution (Cuzzi et al. 2003; Pignatale et al. 2018). The loss of CAIs, however, is not sufficient to explain the degree of Al- and Ca-depletion in ordinary and enstatite chondrites. The relative amount of Al that is present in CAIs is less than 10% for carbonaceous chondrites (Hezel et al. 2008), so even losing all of CAIs accounts for less than half of observed depletion. Instead, the other constituents of chondrites

* Corresponding author.
E-mail address: ymiya@caltech.edu (Y. Miyazaki).
[1] Present address: Division of Geological and Planetary Sciences, California Institute of Technology, Pasadena, CA 91125 USA.

https://doi.org/10.1016/j.icarus.2021.114368
Received 17 October 2020; Received in revised form 7 February 2021; Accepted 9 February 2021

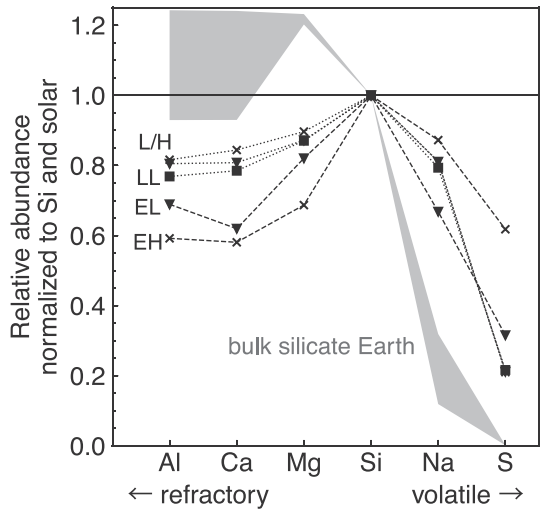

Fig. 1. Abundances of Al, Ca, Mg, Na, and S normalized by Si and by the solar composition for chondrites and the bulk silicate Earth. BSE (gray shaded), ordinary (dotted), and enstatite chondrites (dashed) are shown. Chondrite subgroups are denoted by labels and markers for EH (cross), EL (triangle), H (cross), L (triangle), and LL (square). Data for BSE are taken from Lyubetskaya and Korenaga (2007) and McDonough and Sun (1995), and those for chondrites are from Wasson and Kallemeyn (1988).

including chondrules must have formed in regions where refractory elements were already somehow depleted (Scott and Krot 2014). The depletion of Mg is even more difficult to explain. The proportions of Mg and Si that are present in CAIs are less than a few percent, and the loss of CAIs cannot account for the observed 10–20% depletion in Mg. Some attribute the depletion of Mg in enstatite chondrites to some secondary process (Lehner et al. 2013), but such an explanation may not be universally applicable because the proposed secondary process is unlikely to have taken place in ordinary chondrites, which also exhibit similar but weaker Mg-depletion (Fig. 1; Wasson and Kallemeyn 1988).

One possible explanation for the depletion of refractory elements is that Al-, Ca-, and Mg-rich minerals are all preferentially delivered to the inner region of the Solar System, whereas the transport of other minerals is prohibited by evaporation (Miyazaki and Korenaga 2017). Al- and Ca-rich minerals have condensation temperatures of 1600–1800 K at 10^{-3} atm, whereas the major component of silicate minerals, enstatite ($MgSiO_3$), condenses below 1400 K (Grossman 1972; Lodders 2003). Al- and Ca-rich minerals can thus survive the inward transport within a hot region, which may result in a larger loss of Al and Ca compared to Si. On the other hand, fractionation between Mg and Si is likely to be driven by the radial transport of forsterite (Mg_2SiO_4), which has a larger Mg/Si ratio than enstatite. The preferential loss of forsterite is considered to be consistent with the mineral assemblage of enstatite chondrites (Petaev and Wood 1998; Grossman et al. 2008). The condensation temperature of forsterite, however, is higher than that of enstatite by only ~100 K, and with such a small temperature difference, it is not obvious whether forsterite can decouple from enstatite to create the depletion of Mg observed in ordinary and enstatite chondrites. We need an astrophysical model to investigate how and where the loss of these minerals can happen within protoplanetary disks.

Minerals not only evaporate, but they also react with the surrounding gas and change their compositions while advecting through the protoplanetary disk. When enstatite drifts inward, for instance, it first dissociates to yield forsterite and SiO before its complete evaporation. Solving for the physical and chemical evolution of the disk simultaneously is, therefore, a key to modeling fractionation among major elements. In this study, we incorporate condensation theory into the astrophysical model of protoplanetary disks in a self-consistent manner. Our model tracks actual gaseous and mineral species, whereas previous disk models described the chemical evolution using simplified species, by grouping several minerals into a single species as "silicates" or "volatiles" (Ciesla and Cuzzi 2006; Estrada et al. 2016; Pignatale et al. 2018; Vollstaedt et al. 2020). These simplified species are assumed to evaporate above their condensation temperatures, but such a crude treatment cannot account for fractionation between Mg and Si. Also, by using actual mineral species, we can better predict the Al/Si and Ca/Si ratios because Al- and Ca-rich minerals contain some amount of Mg and Si. Grouping minerals into Al- and Ca-bearing refractories and Mg- and Si-bearing silicates cannot accurately estimate the evolution of Al/Si and Ca/Si ratios.

With our new approach, we show that fractionation between Mg and Si can indeed be driven by the loss of forsterite in the region where enstatite evaporates under certain conditions. For the cases where Mg-depletion occurs, the loss of forsterite accompanies an enrichment in Mg just inside the region with Mg-depletion, together with the high concentration of pebbles. The streaming instability may potentially be triggered in the region, and planetesimals with two different major element compositions, corresponding to enstatite chondrite and Earth, could originate from the region around the evaporation front of enstatite. This indicates a link between Mg-Si fractionation and the formation of silicate planetesimals, and thus our model could be used to bridge the fields of astrophysics and cosmochemistry.

2. Model

Our model solves for the radial motions of all species using the following advection-diffusion equation (Estrada et al. 2016; Desch et al. 2017), which includes an additional term, S_i (Aguichine et al. 2020), to account for condensation ($S_i > 0$) and evaporation ($S_i < 0$):

$$\frac{\partial \Sigma_i}{\partial t} = \frac{1}{r}\frac{\partial}{\partial r}\left(-rv_i\Sigma_i\right) + \frac{1}{r}\frac{\partial}{\partial r}\left(r\nu\Sigma\frac{\partial}{\partial r}\left(\frac{\Sigma_i}{\Sigma}\right)\right) + S_i \tag{1}$$

The first term on the right hand side describes advection, and the second term is dissipation based on the concentration gradient, where Σ_i denotes the surface density of species i, t is time, r is the distance from the Sun, v_i is the advection velocity, ν is viscosity, and Σ is the total surface density. The species in our model include actual gaseous species and minerals, and the source term S_i is calculated through Gibbs energy minimization (Miyazaki and Korenaga 2017; see Section 2.5 for details), allowing us to model various kinds of fractionation including the one between Mg and Si. We do not specify the condensation temperature of each species a priori. Condensation temperatures are naturally determined through Gibbs energy minimization, and their values vary with pressure and composition.

For each chemical species, gas, dust, and pebble components are considered, which are used to represent different dynamical behaviors, and Eq. (1) is solved separately for each component and species. Pebbles represent solids that grow larger than the main dust population, which thus have a larger advection velocity than the dust component. This is motivated by the recent findings that some fraction of solids grow orders of magnitude larger than the fragmentation barrier (Windmark et al. 2012; Estrada et al. 2016); larger grains have lower probabilities of destruction and can grow by colliding with smaller grains. The most notable role of such pebbles is their ability to transfer minerals towards the inner region because of large grain sizes and thus large drift velocities (Ciesla and Cuzzi 2006; Ciesla 2008). The size and mass fraction of pebbles are therefore important in characterizing fractionation among major elements, but they depend on various factors including turbulent viscosity, specific energies for bouncing and fragmentation, and the efficiency of erosion (Zsom et al. 2010; Windmark et al. 2012; Estrada et al. 2016). In this study, instead of solving the collisional coagulation equation (Dullemond and Dominik 2005), we characterize the formation of pebbles using two parameters: the time scale for the dust to grow into pebbles, $\tau_{d\to p}$, and the normalized grain size of pebbles, St_p, to

understand the role of pebbles on major element chemistry. For simplicity, we assume a single grain size for the pebble component, and the consequence of having a distribution in grain size is discussed later. We investigate under what conditions protoplanetary disks can create a depletion pattern consistent with ordinary and enstatite chondrites.

2.1. Disk evolution model

We constructed a 1 + 1D disk evolution model to track the temporal and spatial evolution of the disk temperature, pressure, and the surface densities and chemical compositions of the three components: gas, dust, and pebble. Our model considers mass transport only in the radial direction, but the thermal and compositional structures in the vertical direction are taken into account (Miyazaki and Korenaga 2017; see Appendix A.1). At each timestep, disk dynamics, dust growth and transport, and Gibbs energy minimization are solved simultaneously, which keeps the thermal and compositional structures of the protoplanetary disk self-consistent. Our model considers a system spanning from 0.05 to 30 AU using 600 bins equally distributed over the entire system, and each bin contains the information on temperature, pressure, and the mass and composition of three components. We use a timestep of 0.01 year to solve for the evolution of surface densities (Eq. (1)), whereas the thermal structure and equilibrium among different components are updated every 25 years. The initial disk mass is set to 0.21 $M_{\odot}$, with a surface density inversely proportional to the heliocentric distance. Varying the disk mass would shift the initial location of the evaporation front of enstatite, but it would not affect that Mg-depletion and pebble concentration occur around the evaporation front.

2.2. Thermal structure

The thermal structure of the disk is solved using energy balance between blackbody radiation and viscous dissipation:

$$\sigma_B T_e^4 = \frac{9}{8}\nu\Sigma\Omega_K^2 \tag{2}$$

where σ_B is the Stefan-Boltzmann constant, T_e is the effective temperature, and Ω_K is the local Keplerian angular velocity. The midplane temperature, T_m, is then calculated from the effective temperature by integrating the radiative transfer equation (Miyazaki and Korenaga 2017),

$$\frac{dT}{dz} = -\frac{3\overline{\kappa_R}\rho_g}{16\sigma_B T^3}F_z \tag{3}$$

from the disk surface to the midplane, where z is the height from the midplane, $\overline{\kappa_R}$ is the Rosseland mean opacity, ρ_g is the gas density, and F_z is the vertical radiative flux (see Appendix 5.1 for details). The protoplanetary disk is also heated by the solar irradiation, but its effect on the midplane temperature is negligible in regions where silicates are evaporated. Because its heat is both deposited and re-radiated near the disk surface, it produces zero net vertical flux throughout the disk. Therefore, the solar irradiation does not contribute to creating a thermal gradient towards the midplane ($F_z = 0$). A temperature high enough to evaporate silicates is maintained by viscous dissipation, whose energy is radiated towards the surface from the midplane.

The viscosity is scaled using the α-prescription (Shakura and Sunyaev 1973) as $\nu = \alpha c_s^2/\Omega_K$, where c_s is sound velocity, which is proportional to $\sqrt{T}$. The source and degree of turbulence have been an active area of research, and recent findings suggest that a certain degree of turbulence exists throughout the disk. Because the focus of our model is in the early stage of a protoplanetary disk, both magneto-rotational instability and pure hydrodynamic turbulence are considered as the source of turbulent viscosity (Bai and Stone 2013; Nelson et al. 2013; Stoll and Kley 2014). We thus adopt 10^{-2}, 10^{-3}, and 10^{-4} as the possible values of α.

2.3. Dynamic evolution

For each species i in the gas and dust components, its surface density Σ_i is solved using a 1D radial disk evolution model described in Eq. (1). The advection velocity v_i is calculated separately for the gas and dust components. For the gas component,

$$v_i^{\rm gas} = -\frac{3}{\sqrt{r}\Sigma}\frac{\partial}{\partial r}\left(\nu\sqrt{r}\Sigma\right) \tag{4}$$

is adopted, and for the dust component, the drift velocity is added to $v_i^{\rm gas}$:

$$v_i^{\rm dust} = v_i^{\rm gas} + \frac{\rm St}{1+{\rm St}^2}\frac{1}{\rho_{g,0}\Omega_K}\frac{dP}{dr} \tag{5}$$

where St is the normalized stopping time, $\rho_{g,0}$ is the gas density at the disk midplane, and P is pressure. The normalized stopping time, also known as the Stokes number, is the ratio of stopping and eddy turnover times:

$${\rm St} = \frac{\rho_m}{\rho_{g,0}}\frac{s}{c_s}\Omega_K \tag{6}$$

where ρ_m is the material density of dust grains, and s is the grain size. The gas density $\rho_{g,0}$ is calculated from the surface density using

$$\rho_{g,0} = \frac{1}{\sqrt{2\pi}}\frac{\Sigma_g}{c_s/\Omega_K} \tag{7}$$

where Σ_g is the gas surface density, calculated as the total surface density of all gas species. Pressure is calculated using the ideal gas law as

$$P = \frac{\rho_{g,0}}{m_g}k_B T \tag{8}$$

where m_g is the mean molecular weight and k_B is the Boltzmann constant. The drift velocity of pebbles is calculated using Eq. (5) as well, but with a different Stokes number. The Stokes number is a function of grain size, and, in this study, we set the value of the Stokes number, rather than using the actual grain size, to describe characteristic grain sizes of the distribution (Section 2.4). For simplicity, the Stokes number of pebbles is assumed to be constant throughout the disk, although it may vary depending on the local dust density and the strength of minerals constituting pebbles.

2.4. Grain size distribution

The distribution of grain size of solid particles is necessary to calculate opacity (Appendix A.1) and the advection velocity of the dust component. Following Estrada et al. (2016), we assume that the dust mass distribution follows a power law ($f(m) \propto m^{-q}$) as a consequence of a balance between coagulation and fragmentation. Previous studies have shown that nearly constant mass is distributed per decade in a turbulent disk (Weidenschilling 2000; Brauer et al. 2008; Birnstiel et al. 2010), and we use the exponent of $q = 11/6$, which corresponds to slightly more mass being carried by larger grains. The minimum grain size in the distribution is set to 0.1 μm, whereas the Stokes number of the largest grain, $\rm St_{max}$, is characterized by the fragmentation barrier and is described using the following scaling law (Estrada et al. 2016):

$${\rm St_{max}} = \frac{Q_*}{\alpha c_s^2} \tag{9}$$

where Q_* is the specific energy of fragmentation. We adopt a value of 1 $\rm m^2/s^2$ for Q_*, corresponding to collisions of weak silicate particles at low relative velocity (Stewart and Leinhardt 2009). Electrostratic and bouncing barriers (Zsom et al. 2010; Okuzumi et al. 2011) have also been proposed to inhibit the growth, but they are not impermeable barriers and merely slow the growth of particles. Because particles are

likely to grow until they reach the fragmentation barrier given a long enough time, the maximum grain size of s_{max}, calculated from St_{max}, is adopted in our model.

Pebbles, on the other hand, are generated from the dust component according to the accretionary timescale $\tau_{d\to p}$ (Cassen 2001; Ciesla 2008):

$$\dot{M}_p(r) \propto \frac{M_d}{\tau_{d\to p}} \tag{10}$$

where $\tau_{d\to p}$ is assumed to vary inversely proportional to the local Kepler angular velocity ($\tau_{d\to p}(r) = \tau^0_{d\to p} \cdot \Omega_K(1\ \mathrm{AU})/\Omega_K(r)$). The timescale can be related to the ratio between dust and pebble masses because the production of pebbles and their loss through radial drift become quickly balanced in most regions. Our model produces a roughly constant pebble/dust ratio in the region not affected by the presence of the evaporation front. This is consistent with more detailed grain growth models (Brauer et al. 2008; Estrada et al. 2016), and we thus regard that this implementation is sufficient for understanding the major element chemistry to first order. Although the fragmentation of pebbles is not implemented in our model, its effect is captured through the accretionary timescale, which can be regarded as the net pebble production rate. This simplification would not affect the final compositional structure because equilibrium between gas and solid is reached within the drift timescale (see Section 2.5 for details). For $\tau^0_{d\to p}$, we tested values of 10^2 and 10^3 yr in our model (Appendix A.2), corresponding to the pebble/dust mass ratio of $\sim 10^{-1}$ and $\sim 10^{-2}$, respectively, for pebbles with $St_p \sim 0.005$. The size of pebbles is estimated from previous studies (Brauer et al. 2008; Estrada et al. 2016), and the values of 0.005 and 0.05 are tested in this study.

2.5. Gibbs energy minimization

We assume the solar composition for the initial composition, although only major elements (H, C, O, Na, Mg, Al, Si, S, Ca, and Fe) are considered in this study. For gas species, Al, AlOH, Ca, CH_4, CO, CO_2, Fe, H, H_2, H_2O, H_2S, Mg, Na, NaOH, O_2, Si, SiO, and SiS are considered, and for mineral species, corundum (Al_2O_3), melilite (solid solution between gehlenite ($Ca_2Al_2SiO_7$) and akermanite ($Ca_2MgSi_2O_7$)), olivine (solid solution between forsterite (Mg_2SiO_4) and fayalite (Fe_2SiO_4)), orthopyroxene (solid solution between enstatite ($MgSiO_3$) and ferrosilite ($FeSiO_3$)), spinel ($MgAl_2O_4$), anorthite ($CaAl_2Si_2O_8$), diopside ($CaMgSi_2O_6$), albite ($NaAlSi_3O_8$), metallic iron (Fe), troilite (FeS), and graphite (C) are considered. Thermodynamic data for silicate minerals are taken from Robie and Hemingway (1995), and the rest of the species are from the JANAF Thermochemical Tables. We use the method of Miyazaki and Korenaga (2017) to perform Gibbs energy minimization. Thermodynamic data are available for protoplanetary disk conditions, and condensation temperatures calculated from the database are shown to match the trend observed in meteorites (e.g., Larimer 1967; Grossman 1972; Lodders 2003).

Gibbs energy minimization is applied to the total composition of the gas and dust components, and the source term S_i in Eq. (1) reflects changes in the amount of gas and mineral species. The same is applied to equilibrium between the gas and pebble components because, as explained later, pebbles equilibrate with the surrounding gas within a short duration. When pebbles do not evaporate entirely, we assume that the Stokes number of pebbles remains constant and instead decrease the number of pebbles, although, in reality, pebbles would become either smaller or more porous upon evaporation, lowering the Stokes number. An equivalent treatment is seen in previous studies, in which pebbles are regarded as aggregates of chemically distinct monomers (e.g., Estrada et al. 2016). We intend to study the effect of evaporation on pebbles in future work.

Gibbs energy minimization assumes that equilibrium between the gas and solid components is achieved. In this study, Gibbs energy minimization is performed every 100 years, which is estimated to be shorter than equilibrium timescale. In addition to grain size, equilibrium timescale depends on whether minerals are evaporating or condensing to reach equilibrium. The evaporation experiments of silicates show that mm-size minerals evaporate within a few years at the longest (Kuroda and Hashimoto 2002; Takigawa et al. 2009), and thus cm-size pebbles would likely equilibrate with the surrounding gas within 100 years. It is noted that these experiments are conducted under pure H_2 gas, but including other Si-bearing gases is not expected to affect the speed of evaporation as long as minerals are subjected to a temperature sufficiently higher than their condensation temperatures. Pebbles experience higher temperature as they drift inward, so evaporation would most likely be completed within in the model timestep. On the other hand, the timescale of condensation remains uncertain because the nucleation rate has not been quantified due to the extreme difficulty in conducting a nucleation experiment in high temperatures and low pressures (Nagahara 2018). Most condensation in our model, however, should occur as heterogeneous nucleation in regions where other minerals exist, so the timescale is suspected to be comparable with the case of evaporation. If the condensation of minerals were to be hindered by kinetics, evaporated silicate gases would diffuse to the outer region without condensing, and the degree of Mg-depletion would become weaker than our model results.

Equilibrium timescale may be longer in the colder outer region, but reactions of silicates, including evaporation and condensation, are mostly absent outside the evaporation front of albite. A notable exception is the formation of fayalite from forsterite and metallic iron, which proceeds at lower temperatures (Fig. 2D). Because the Fe-Mg interdiffusion in olivine is known to be negligible below ~600 K (Fedkin and Grossman 2006; Grossman et al. 2008), the FeO content in silicates predicted in the outer region may be overestimated. This, however, would not affect the compositional structure in the inner region, which is the main focus of this study.

3. Results

3.1. Fractionation between Mg and Si

Our model dynamically tracks the evolution of major element chemistry within protoplanetary disks. The physical evolution of the disk is similar to previous models (Ciesla and Cuzzi 2006; Estrada et al. 2016), where temperature gradually decreases, and solid is enriched in the inner region as pebbles are transported inward by radial drifting (Fig. 2A, B). Mineral assemblages predicted in our model, however, indicate the new aspects of the protoplanetary disk chemistry. They change mostly as a function of temperature, but in regions where minerals evaporate, constituent elements are enriched by the transport of pebbles, altering mineral compositions. In particular, just outside the evaporation front of enstatite, which hereafter refers to the region where enstatite evaporates, the ratio of forsterite (olivine) to enstatite (orthopyroxene) decreases from ~0.17 to ~0.05 during the first 0.1 Myr of evolution (Fig. 2C, D). Because the molar Mg/Si ratio of forsterite is 2:1 and is larger than that of enstatite, fractionation between forsterite and enstatite results in the depletion of Mg (Fig. 3A, C).

Such enrichment of enstatite can be explained by the preferential loss of forsterite, which is driven by the difference in condensation temperatures between forsterite and enstatite. Because enstatite evaporates ~100 K lower than forsterite, the evaporation front of enstatite encloses the region where forsterite remains as solid (Figs. 2C, 4). While enstatite evaporates, condensed forsterite continues to be incorporated into pebbles and is transported further to the inner region, leaving the region outside the evaporation front to be depleted in Mg. Pebbles thus hold a key to creating fractionation; our model produces negligible fractionation when the pebble/gas ratio is low. A shorter time scale for pebble formation produces a higher surface density of pebbles, resulting in a greater degree of fractionation (Table 1).

A high concentration of pebbles is required because chemical

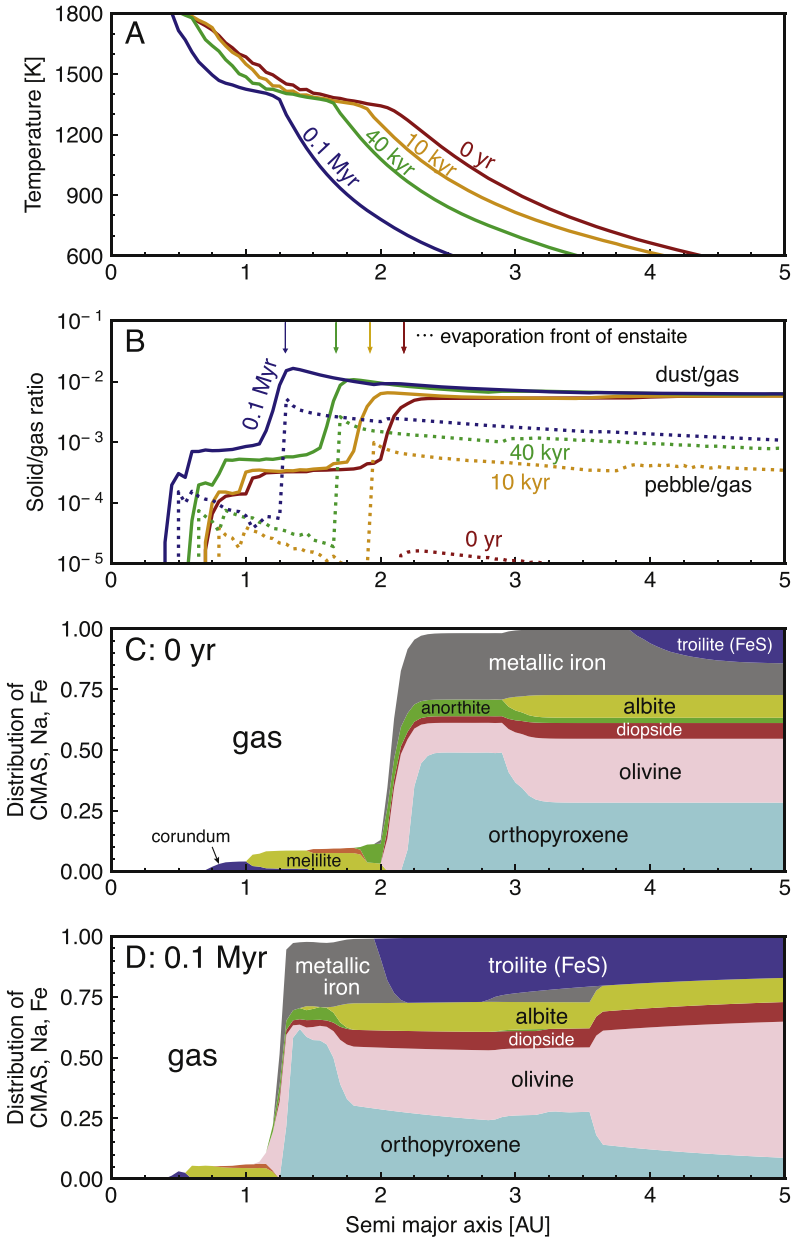

Fig. 2. Snapshots of disk evolution for α=10^{-3}, St_p=0.005, and $\tau^0_{d\to p}$=100 yr. (A) Temperature and (B) the solid/gas ratio are shown, and colors denote 0 kyr (red), 10 kyr (orange), 40 kyr (green), and 0.1 Myr (blue). Solid and dotted lines in (B) indicate the ratios of dust/gas and pebble/gas, respectively, and arrows are the evaporation front of enstatite at different times. (C, D) Predicted mineral assemblages of the system at (C) t=0 yr and (D) t=0.1 Myr. The relative molar amount of solid-composing elements, Na, Mg, Al, Si, Ca, and Fe, in the solid phase is plotted as a function of heliocentric distance, where colors denote different mineral phases: corundum (Al_2O_3, dark blue), melilite ($Ca_2Al_2SiO_7$, yellow), orthopyroxene ($(Mg,Fe)SiO_3$, cyan), olivine ($(Mg,Fe)_2SiO_4$, pink), diopside ($CaMgSi_2O_6$, red), anorthite ($CaAl_2Si_2O_8$, green), albite ($NaAlSi_3O_8$, yellow), metallic iron (Fe, gray), and troilite (FeS, purple). (For interpretation of the references to colour in this figure legend, the reader is referred to the web version of this article.)

heterogeneity created by pebble transport can be eliminated by vigorous turbulence within the protoplanetary disk. Because enstatite and forsterite evaporate at nearby regions (Fig. 2C, D), fractionation between Mg and Si is more vulnerable to turbulence and is easier to be re-homogenized than fractionation between other elements. We use the α-prescription of turbulent viscosity ($\nu = \alpha c_s^2/\Omega_K$; Shakura and Sunyaev 1973) to describe the strength of turbulence. For simplicity, the diffusivity and viscosity are assumed to be the same in this study (e.g., Estrada et al. 2016). For the cases with $\alpha = 10^{-2}$, which is the upper estimate for protoplanetary disks (Davis et al. 2010; Armitage 2011), fractionation between Mg and Si is too limited (~2%; Figs. 3E, 5D) to explain what is observed in chondrites (~10–18%) (Fig. 1; Wasson and Kallemeyn 1988). If the fractionation cannot be explained by other mechanisms, then, our model may be used to constrain astrophysical parameters using cosmochemical observations (see Section 4.1 for details).

The other parameter investigated in our model is the size of pebbles, which is characterized by the normalized grain size St_p. The advection velocity of pebbles, being proportional to their grain size for St_p<1, is directly related to the ability to produce chemical heterogeneity. Therefore, larger pebbles could induce more fractionation between Mg and Si (Figs. 3C, 6D) even with a lower pebble/gas ratio. When the other parameters are the same, however, a larger pebble size lowers the concentration of pebbles because pebbles drift faster and are lost towards the Sun before their concentration increases (Fig. 6B, dotted lines). In regions not affected by condensation and evaporation, the pebble/gas ratio is controlled by a balance between the production of pebbles and their loss towards the inner region by radial drift. Therefore, having a large pebble size does not always result in a higher degree of depletion (Al/Si and Na/Si in Fig. 3A, C).

A dynamic balance between turbulent mixing and forsterite transport by pebbles maintains Mg-depletion behind the evaporation front of enstatite (Fig. 3). The degree of Mg-depletion first grows with time at the beginning of the evolution, but once turbulent mixing and pebble

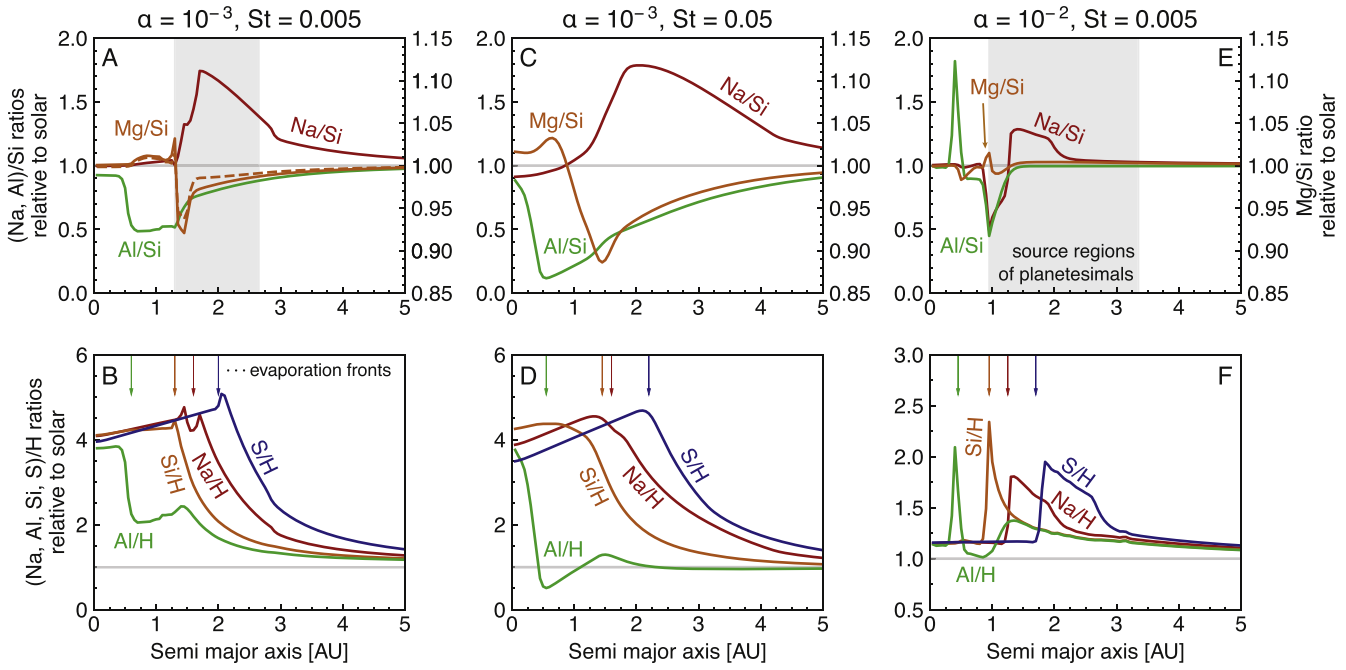

Fig. 3. Modeled profiles of system composition in terms of the relative abundances of (A, C, E) Na (red), Mg (orange), and Al (green) normalized by Si and the composition of solar composition, and (B, D, F) Na (red), Al (green), Si (orange), and S (blue) normalized by H and the solar composition. These plots show the profile after 0.1 Myr of evolution for (A, B) and 40 kyr for (C). The parameters used to create this figure are the same as Fig. 2 for (A, B). Cases when (C, D) the normalized pebble size is 10 times larger and when (E, F) the turbulent viscosity is 10 times larger are also shown. The dotted line in (A) indicates the case where the re-condensation of solid-composing elements onto pebbles is neglected. Gray lines in all panels denote unity, corresponding to an unfractionated value. Regions with the pebble/gas ratio larger than 0.3%, where planetesimals may form by the streaming instability, are shaded in (A, E). In (C), the pebble/gas ratio is too low to trigger the streaming instability, so no region is shaded. In (B, D, F), the evaporation fronts of corundum (green), enstatite (orange), albite (red), and troilite (blue) are denoted by arrows. These minerals are the major host phases of Al, Si, Na, and S, respectively, at the time of evaporation. (For interpretation of the references to colour in this figure legend, the reader is referred to the web version of this article.)

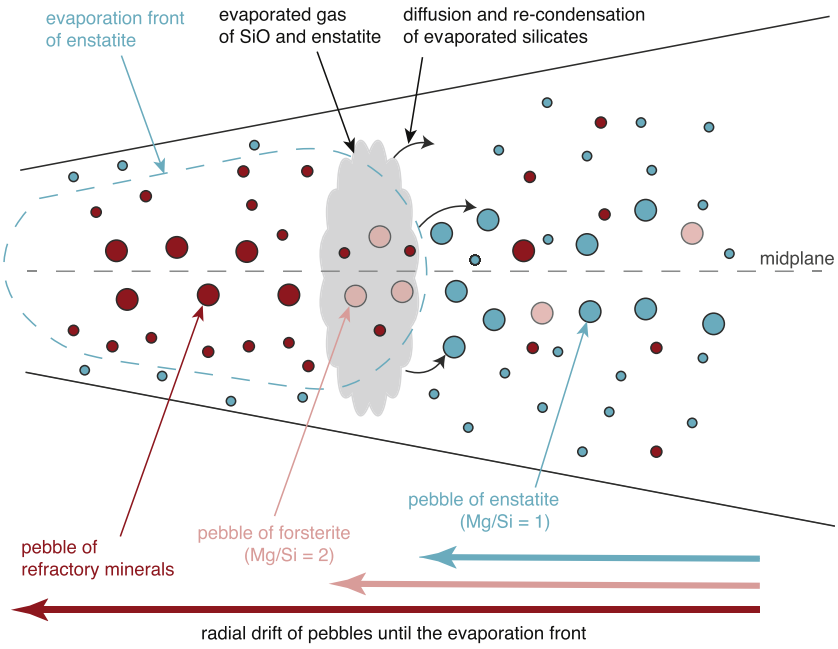

Fig. 4. A cartoon illustrating the evolution of the protoplanetary disk around the condensation front of enstatite. Whereas the transport of solid grains composed of enstatite is prohibited by its evaporation front, more refractory minerals including corundum, melilite, and forsterite are transported further inside, creating depletion in Al, Ca, and Mg outside the front. Colors indicate the composition of dust grains and pebble: refractory minerals (corundum and melilite; red), forsterite (pink), and enstatite (cyan). (For interpretation of the references to colour in this figure legend, the reader is referred to the web version of this article.)

transport reaches equilibrium, the minimum Mg/Si ratio remains unchanged (Fig. 7C). As the disk cools down, the dip in the Mg/Si profile moves inward together with the front, and fractionation between Mg and Si is barely observed outside the front (Fig. 7C). Therefore, some mechanism that conserves Mg-depletion until the later stage of evolution is needed to explain the observed Mg-Si fractionation in ordinary and enstatite chondrites. A promising candidate to preserve the fractionation is planetesimal formation by the streaming instability (Johansen et al. 2007, 2009). Once solid particles grow into km-size bodies, they would not be affected by turbulent mixing or radial

Table 1
Summary of all cases tested in this study. Modeling results are evaluated from three perspectives: a large enough pebble/gas ratio (>5.0 × 10^{-3}), the Mg-depletion (<0.9), and Al-depletion (<0.8), the latter two of which are consistent with ordinary chondrites. All three criteria are met only when turbulence is sufficiently weak ($\alpha \leq 10^{-3}$), the grain size of pebbles are in the right range ($St_p \sim 0.01$), and the time scale for pebble formation is short enough ($\tau^0_{d\to p} \leq 100$ yr).

α	St_p	$\tau^0_{d\to p}$	Σ_p/Σ_g	Mg/Si	Al/Si
10^{-2}	0.0005	10^2	∘	×	×
10^{-2}	0.005	10^2	∘	×	∘
10^{-2}	0.05	10^2	×	×	∘
10^{-2}	0.005	10^3	×	×	×
10^{-2}	0.05	10^3	×	×	×
10^{-3}	0.0005	10^2	∘	×	∘
10^{-3}	0.005	10^2	∘	∘	∘
10^{-3}	0.05	10^2	×	∘	∘
10^{-3}	0.005	10^3	×	×	∘
10^{-3}	0.05	10^3	×	×	×
10^{-4}	0.005	10^2	×	∘	∘
10^{-4}	0.05	10^2	×	∘	∘
10^{-4}	0.005	10^3	×	∘	∘
10^{-4}	0.05	10^3	×	∘	∘

drifting during the subsequent evolution. The onset of the streaming instability is discussed in detail later.

3.2. Depletion of other refractory elements

Highly refractory elements including Al and Ca show a larger depletion compared to Mg. The condensation temperatures of Al- and Ca-bearing minerals such as corundum and melilite are higher than that of enstatite by 200–300 K, which corresponds to a ~1 AU difference in the distance from the Sun for the case shown in Fig. 2. Because the length scale of turbulent diffusion is shorter than 1 AU, turbulent mixing does not eliminate fractionation among Al, Ca, and Si, resulting in a larger degree of depletion compared to Mg.

The Al/Si ratio of the system composition, normalized by the solar composition, is lower than unity in the inner region of the disk, and this is owing to different degrees of enrichment in Al- and Si-bearing minerals. Solid-composing elements are enriched at the evaporation front of each mineral through the continuing transport and evaporation of pebbles, as seen in their concentrations normalized by H (Fig. 3B, D, and F). The most refractory element in this study, Al, shows enrichment in the region closest to the Sun, and other peaks of enrichment are observed further away from the Sun for elements with higher volatility (Si, Na, and S in the increasing order of volatility). At the evaporation front of enstatite, the Si/H ratio is peaked but not the Al/H ratio, resulting in a decrease in the Al/Si ratio. The enrichment of moderately volatile elements around ~2 AU (Fig. 3A, C, and E) can be explained similarly. The ratio of Na/Si, for example, is higher than unity around the evaporation front of albite because Na is enriched but Si is not. Solids formed further away from the Sun thus would be depleted in Al, Ca, and Mg, but enriched in Na compared to Si.

A Na/Si ratio larger than unity extends outside the evaporation front of albite ($NaAlSi_3O_8$). Na and Si are enriched both inside and outside their corresponding evaporation fronts because disk turbulence diffuses evaporated gas away from the front, and evaporated gas would re-condense as solids as it diffuses across the front. The degree of enrichment decreases further away from their corresponding evaporation front, so the Na/H ratio is larger than the Si/H ratio in the outermost region (Fig. 3B, D, and F). This indicates that planetesimals formed further away from the Sun may have an enrichment in volatiles, including Na, compared to Si.

3.3. Onset of the streaming instability

The region around the enstatite evaporation front has the highest dust concentration inside the snow line due to the inward flux of pebbles from the outer region, so it has a high probability that the instability is triggered therein. Because most silicates in the pebble component evaporate close to the evaporation front of enstatite and their constituting elements do not migrate further inward, the net increase of dust-composing elements is observed around the front. Vaporized silicates diffuse back across the evaporation front and condense into dust grains and pebbles, which enhances the dust and pebble densities outside the front. When the ratio between the surface densities of pebbles and gas reaches ~1.5%, the streaming instability can be triggered, which is a gravitational instability induced by aerodynamic coupling between solids and gas (Johansen et al. 2007, 2009). The pebble/gas ratio in the results is lower than this threshold, yet it is closest to the threshold around the evaporation front of enstatite. The streaming instability would preferentially collect pebble-size particles to create planetesimals, and thus fossilizing fractionation between Mg and Si.

An additional mechanism that enhances the pebble concentration is the direct re-condensation of evaporated solid-composing elements on to pebbles (Fig. 4). With a high pebble density, some fraction of re-condensation would occur on to the surface of pebbles, increasing the pebble/dust ratio outside the front. In our model, we have distributed the amount of re-condensation to the dust and pebble components according to their total surface areas. Solid particles with larger radii, in general, provide smaller surface area than μm-size dust, but pebbles are likely to be porous (Ormel and Cuzzi 2007) and would provide larger surface area than perfect spheres (see Appendix A.3). Previous models have assumed that all of the re-condensed solid turns into the dust of small grain sizes (Ciesla and Cuzzi 2006; Estrada et al. 2016), but this may underestimate the role of pebbles. In terms of chemistry, the degree of Mg-depletion increases by ~40% (Mg/Si going down from 0.93 to 0.9; Fig. 3A), which is comparable to what is observed in ordinary chondrites (Mg/Si~0.9). The re-condensation onto pebbles also affects the pebble density outside the evaporation front. Because the evaporated gas is abundantly supplied from the inner region, the pebble density becomes highest just outside the evaporation front of enstatite (Fig. 8). This effect is stronger with a larger value of α, which produces a larger diffusive flux (Fig. 5B).

With the re-condensation of dust components, the pebble/gas ratio becomes closer to the threshold for the streaming instability inside the snow line (Fig. 2B) than in previous models (Cuzzi and Zahnle 2004; Estrada et al. 2016). The pebble/gas ratio in our model, however, is still lower than the threshold of 1.5%, and given the small pebble size in the early stage of protoplanetary disk evolution, the threshold may even be higher than 1.5% (Yang et al. 2017). Another potential factor that could further increase the pebble density is the "traffic jam" effect, which has been suggested to trigger the streaming instability at the snow line (Drążkowska and Alibert, 2017). Because icy particles are stronger than silicates and grow into a large grain size, pebbles are transported faster outside the snow line than in the inside and thus pile up around the snow line. Although the strength of silicates is likely to be the same across the enstatite evaporation front, a similar phenomenon may take place. Because of a lower dust density, pebbles would be smaller and thus advect slower inside the front. For simplicity, a constant pebble size is adopted in this study, but more detailed grain growth model is desirable for further work.

This suggests a new pathway towards creating planetesimals in the inner region of protoplanetary disks. The region just outside the evaporation front of enstatite, where the pebble/gas ratio is sufficiently high, is dominated by enstatite and is depleted in forsterite (Fig. 2D). Depletion in Al, Ca, and Mg is consistent with ordinary and enstatite chondrites, so planetesimals created by the streaming instability outside the evaporation front of enstatite may serve as a source for these chondrites. While our model is only solved for the first ~0.1 Myr, the onset of the streaming instability would likely continue until the disk becomes too cold to maintain the evaporation front of enstatite. The formation of planetesimals is crucial for preserving depletion in refractory elements,

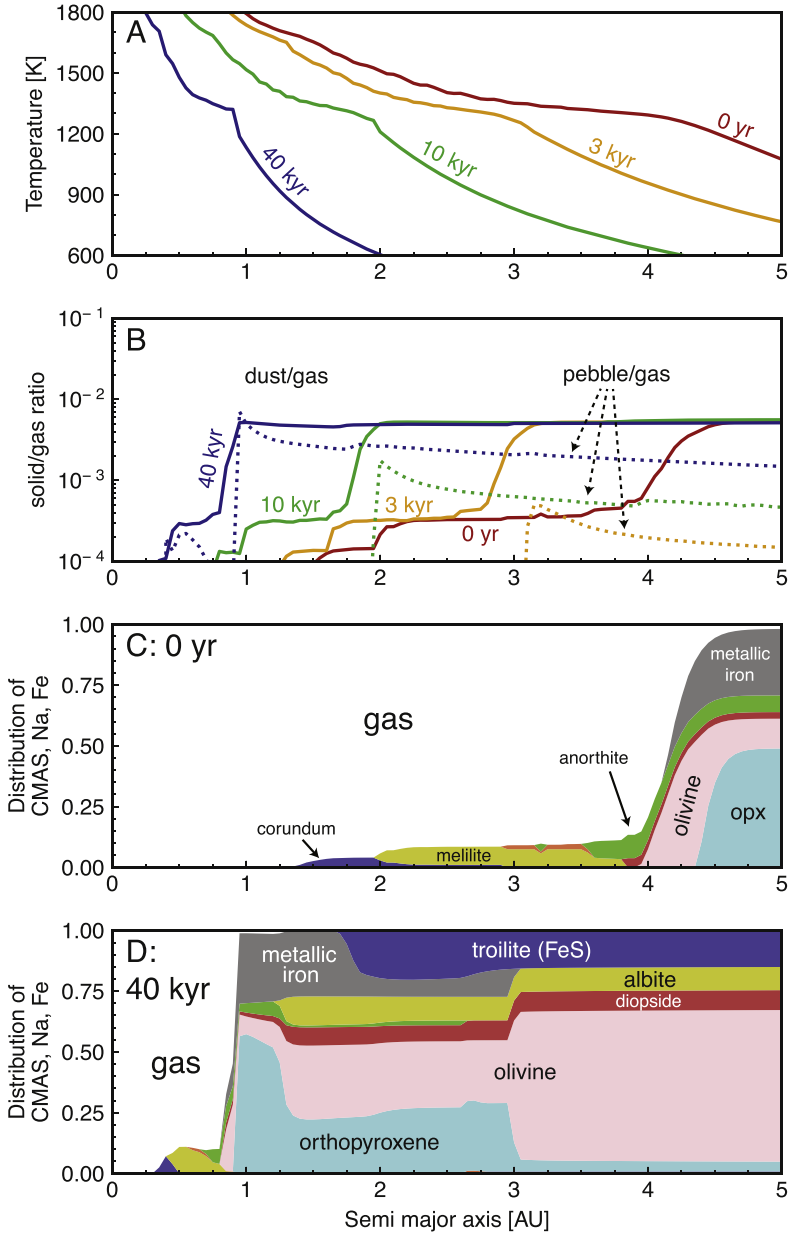

Fig. 5. The same as Fig. 2 but for a larger α (10^{-2}). $St_p = 0.005$ and $\tau^0_{d\to p} = 100$ yr are kept the same. These are the same parameters used in Fig. 3E and F. (A, B) Colors denote 0 kyr (red), 3 kyr (orange), 10 kyr (green), and 40 kyr (blue). Solid and dotted lines in (B) indicate the ratios of dust/gas and pebble/gas, respectively. (C, D) Predicted mineral assemblages of the system at (C) $t = 0$ yr and (D) $t = 40$ kyr. The relative molar amount of dust-composing elements, Na, Mg, Al, Si, Ca, and Fe, in the solid phase is plotted as a function of heliocentric distance, where colors denote different mineral phases. The initial compositional structure shown in (C) differs from what is shown in Fig. 2C because stronger viscous dissipation makes the disk hotter than the case of $\alpha = 10^{-3}$. (For interpretation of the references to colour in this figure legend, the reader is referred to the web version of this article.)

which exists only during the early stage of the disk evolution.

4. Discussion

4.1. Constraints on astrophysical parameters

Our model is so far the only astrophysical model that can produce fractionation between Mg and Si, but even with our model, the fractionation is possible under limited conditions. If the fractionation cannot be explained by other mechanisms, then, our model may be used to constrain astrophysical parameters using cosmochemical observations. To produce Mg-depletion observed in ordinary chondrites, the following three conditions should be met (Table 1): turbulent mixing is sufficiently weak ($\alpha \leq 10^{-3}$), the time scale of pebble formation is short ($\tau^0_{d\to p} \leq 100$ yr), and the grain size of pebbles is in the range corresponding to $St_p \sim 0.01$ (e.g., 10 cm at 2 AU and $t \sim 10^4$ yr). In cases with $\alpha = 10^{-2}$, strong turbulent mixing homogenizes fractionation created by the loss of forsterite (Figs. 3E, 9A). This suggests that magnetorotational instability (MRI) (Balbus and Hawley 1991), for which the suggested value of α is on the order of 10^{-2}, may not have operated in regions around the evaporation front of enstatite. Because the inner region was sufficiently hot and partially ionized during the earlier stage of evolution, MRI has been considered as the primary source of turbulence, but a mechanism that produces weaker turbulence, including purely hydrodynamical turbulence, may better explain Mg-depletion observed in ordinary and enstatite chondrites.

The size of pebbles and the accretionary timescale may also be constrained using the major element chemistry. When the normalized pebble size St_p is smaller than 10^{-3} or the accretionary timescale $\tau^0_{d\to p}$ is shorter than 10^3 years, fractionation between Mg and Si becomes too small to explain the composition of chondrites (Fig. 9C). A larger pebble size, however, is not necessarily favored because it decreases the concentration of pebbles, lowering the possibility of the streaming instability (Youdin and Goodman 2005; Johansen et al. 2009). Although

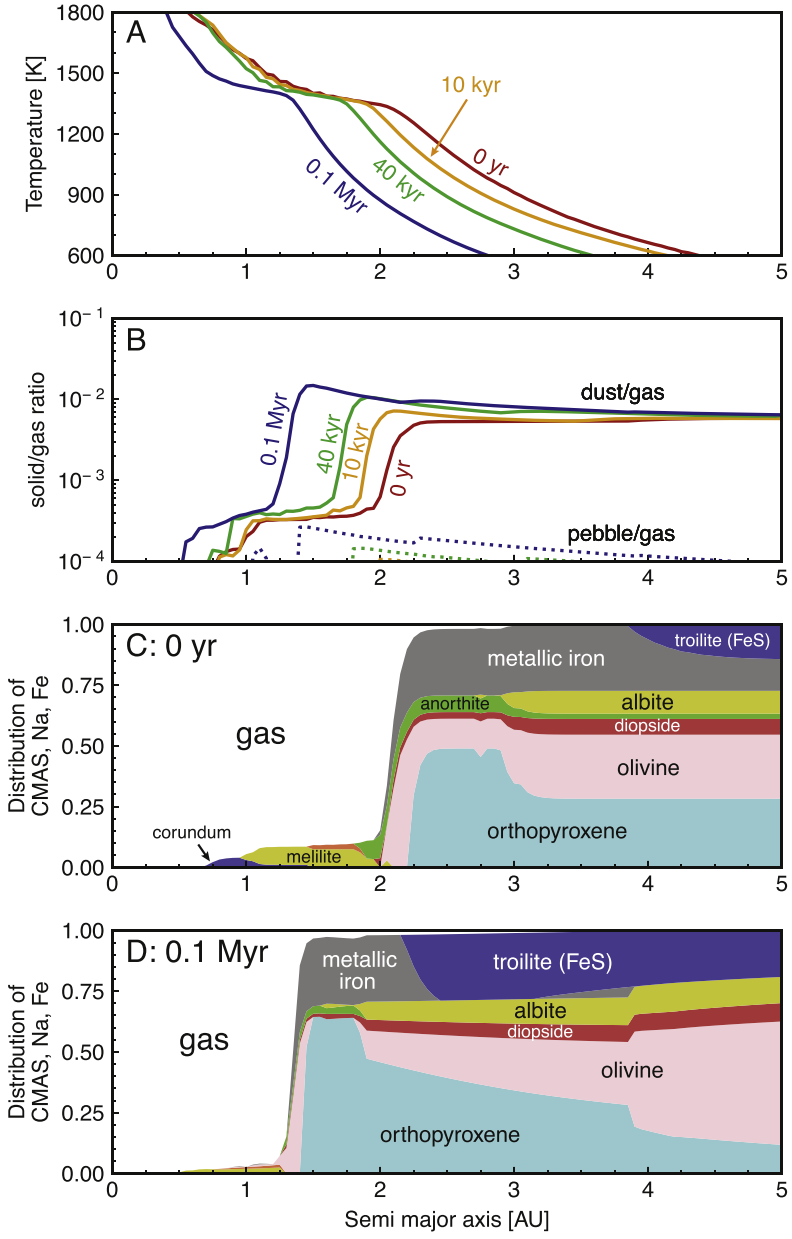

Fig. 6. The same as Fig. 2 but for a larger pebble size St_p (0.05). $\alpha = 10^{-3}$ and $\tau^0_{d\to p} = 100$ yr are kept the same. These are the same parameters used in Fig. 3C and D. (A, B) Colors denote 0 kyr (red), 10 kyr (orange), 40 kyr (green), and 0.1 Myr (blue). Solid and dotted lines in (B) indicate the ratios of dust/gas and pebble/gas, respectively. (C, D) Predicted mineral assemblages of the system at (C) $t = 0$ yr and (D) $t = 0.1$ Myr. The relative molar amount of dust-composing elements, Na, Mg, Al, Si, Ca, and Fe, in the solid phase is plotted as a function of heliocentric distance, where colors denote different mineral phases. (For interpretation of the references to colour in this figure legend, the reader is referred to the web version of this article.)

greater fractionation is observed when St_p exceeds 10^{-2} (Fig. 3C), the pebble/gas ratio becomes smaller than 10^{-3} (Figs. 5B, 6B). The optimal pebble size is likely to be around $St_p \sim 0.005$, where Mg-Si fractionation and the large pebble concentration are both achieved. In reality, the size of pebbles should exhibit a certain degree of distribution, and the compositional evolution should follow somewhere in between the cases of Fig. 3A and C.

4.2. Implications for Enstatite Chondrites

Enstatite and ordinary chondrites both show depletion in refractory elements including Mg, but the degree of depletion is higher for enstatite chondrites. Enstatite chondrites have an additional feature, which points to their formation under reduced conditions. This has been suggested from the existence of sulfides and silica (Larimer and Bartholomay 1979; Grossman et al. 2008) based on the assumption that the mineral assemblages of enstatite chondrites represent direct condensates from the nebular gas. Because sulfides do not condense from the initial solar composition, enstatite chondrites must have condensed either from the gas with a higher C/O ratio than the solar ratio (Larimer and Bartholomay 1979; Grossman et al. 2008) or from the gas enriched in interplanetary dust particles (Ebel and Alexander 2005), both of which produce more reduced condition than the solar composition. The condensates from these compositions, however, also result in the formations of graphite and SiC, neither of which are observed in chondrites. An alternative explanation is that the formation of sulfides is by secondary formation, where oxides reacted with S-rich gas to form sulfides and silica (Lehner et al. 2013).

Based on our modeling results, the hypothesis of sulfidation may have an astrophysical footing. Whereas the S/H ratio of the surrounding nebular gas is only five times the solar abundance, which is insufficient to induce the sulfidation of silicates (Figs. 2D, 5D, and 6D), the transport of troilite-rich materials from the outer region can potentially produce a S-rich reservoir in the terrestrial region. When troilite is delivered

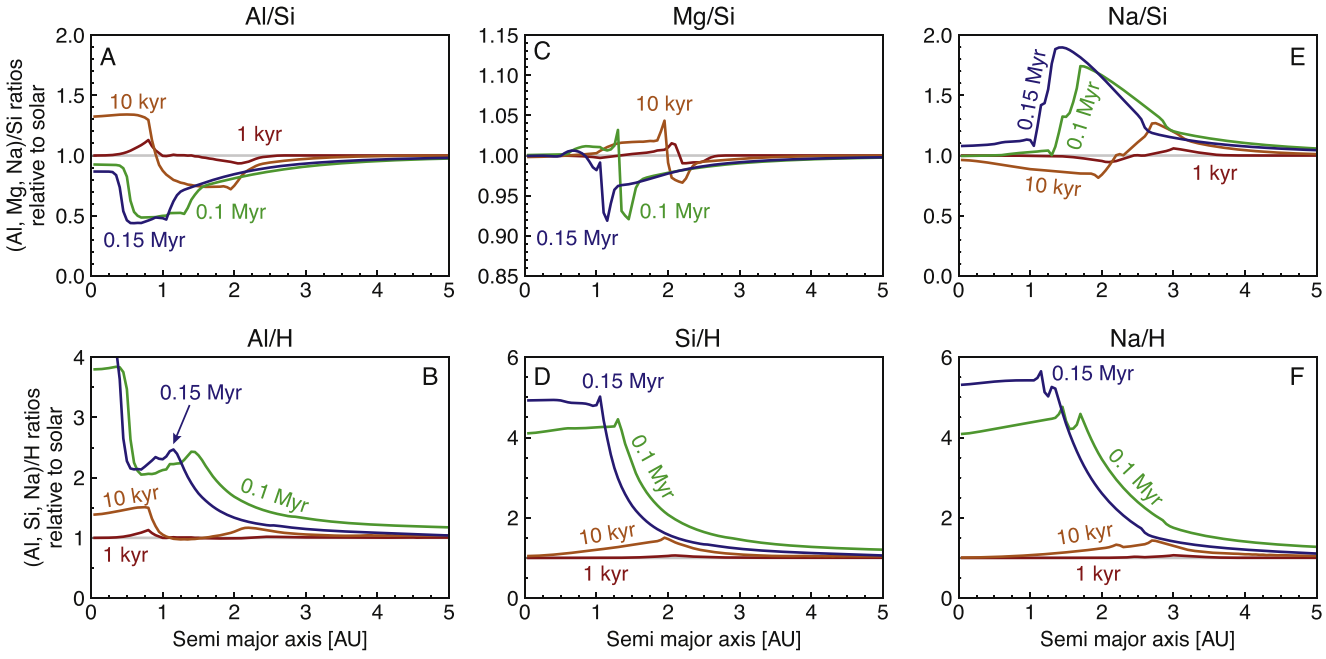

Fig. 7. The evolution of the relative abundance profiles of (A) Al/Si, (C) Mg/Si, and (E) Na/Si normalized by the solar composition, and (B) Al/H, (D) Si/H, and (F) Na/H normalized by the solar composition. Colors denote 1 kyr (red), 10 kyr (orange), 0.1 Myr (green), and 0.15 Myr (blue). The parameters used to create this figure are the same as those used for Figs. 2, 3A, B, and 10. Gray lines in all panels denote unity, corresponding to an unfractionated value. (For interpretation of the references to colour in this figure legend, the reader is referred to the web version of this article.)

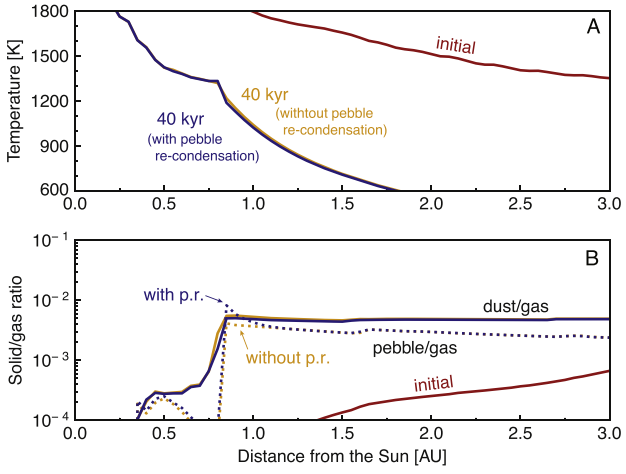

Fig. 8. Snapshots of disk evolution with and without the effect of re-condensation of evaporated gas onto pebbles. The initial condition is denoted in red, and snapshots at 40 kyr for cases with and without the effect of pebble re-condensation (abbreviated as p.r. in (B)) are in blue and yellow, respectively. The parameters used to create this figure are the same as those used for Figs. 3E, F, and 5. Temperature is shown in (A), and solid and dotted lines in (B) indicate the ratios of dust/gas and pebble/gas, respectively. (For interpretation of the references to colour in this figure legend, the reader is referred to the web version of this article.)

during the later stage of evolution, because the surrounding hydrogen gas has already dissipated, reactions between silicate and troilite would produce a higher S/H ratio than observed in the early stage of disk evolution. Such reactions would explain the mineralogy observed in enstatite chondrites, including MgS and CaS (Lehner et al. 2013).

4.3. Evolution after the streaming instability

Planetesimals created outside the evaporation front of enstatite are expected to be depleted in Al, Ca, and Mg, which is consistent with ordinary and enstatite chondrites. During the onset of the streaming instability, it is too hot for Na-bearing minerals to condense, and the initial composition of planetesimals would be depleted in volatile elements including Na and S (Fig. 10, red line). Volatiles are likely to be added to planetesimals after their formation, and the most likely mechanism of acquisition is pebble accretion (Lambrechts and Johansen 2012), by which pebbles efficiently accreted onto planetesimals. For planetesimals of 100 km-size typically formed by the streaming instability (Johansen and Lambrechts 2017), however, they accrete pebbles only at the later stage of evolution when the surrounding gas dissipates and the disk cools down (Fig. 11). Therefore, the composition of planetesimals is unlikely to change during the early stage of evolution, and the addition of Na and S likely happens >0.5 Myr after the onset of the streaming instability. By then, volatile-bearing minerals would be stable in the terrestrial region, although some amount of volatiles would have already been dissipated.

The parent bodies of ordinary and enstatite chondrites may have undergone a similar evolutionary path because the major element compositions of ordinary and enstatite chondrites can be explained by adding volatile-rich pebbles to planetesimals formed outside the evaporation front of enstatite (Fig. 10, orange line). In our calculation with $\alpha = 10^{-3}$, Na- and S-rich pebbles originate from 1.5–3 AU (Fig. 3A), and they were probably transported inward and accreted to planetesimals during the later stage of evolution. It is noted that such pebbles show weaker Al-, Ca- and Mg-depletions than the initial planetesimals, so their accretion slightly weakens the degree of depletion in refractory elements (Fig. 10). Nevertheless, the final composition can still have larger depletion in refractory elements than Na if the planetesimals are greatly depleted in refractory elements when they initially formed by the streaming instability.

Our model, therefore, suggests that the abundances of refractory and

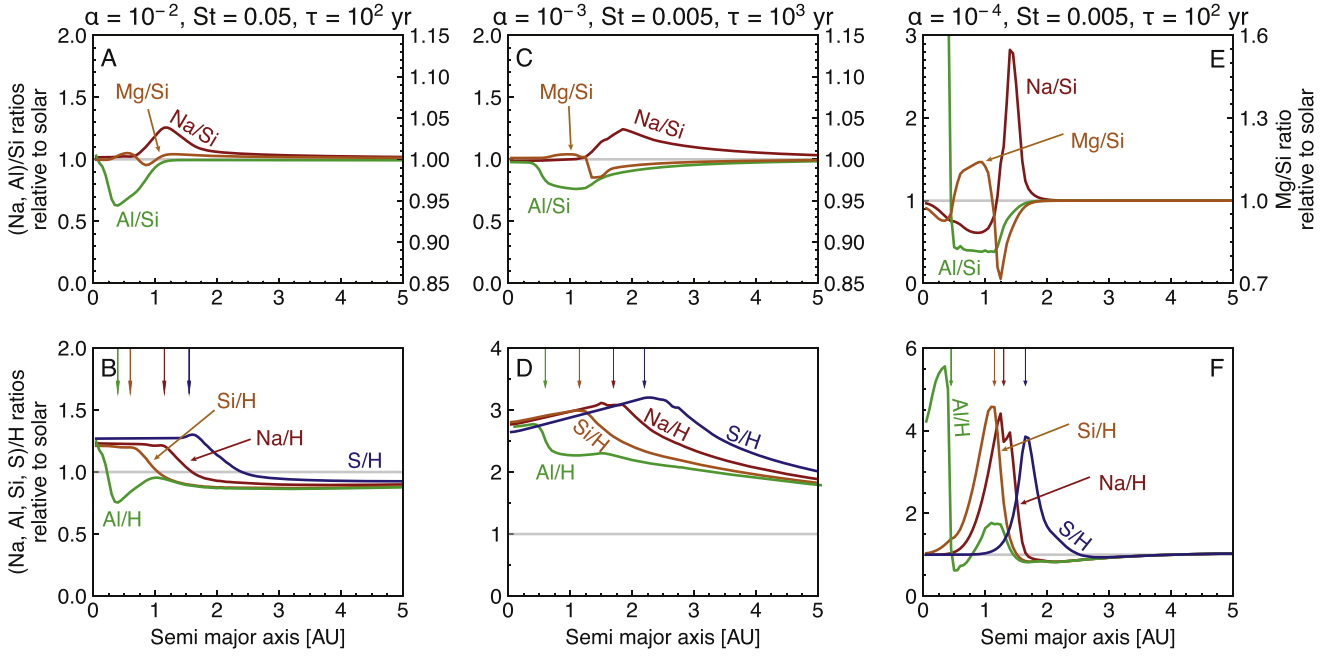

Fig. 9. The same as Fig. 3 but for different sets of parameters. (A, B) $\alpha = 10^{-2}$, $\mathrm{St}_p = 0.05$, $\tau^0_{d\to p} = 100$ yr, (C, D) $\alpha = 10^{-3}$, $\mathrm{St}_p = 0.005$, $\tau^0_{d\to p} = 1000$ yr, and (E, F) $\alpha = 10^{-4}$, $\mathrm{St}_p = 0.005$, $\tau^0_{d\to p} = 100$ yr. Each panel represents the modeled profile of the relative abundance of (A, C, E) Na (red), Mg (orange), and Al (green) normalized by Si and the solar composition, and (B, D, F) Na (red), Al (green), Si (orange), and S (blue) normalized by H and the solar composition. These plots show the profile after (A, B) 40 kyr, (C, D) 0.1 Myr, and (E, F) 20 kyr of evolution. Unlike in Fig. 3, no regions are shaded in this figure because the pebble/gas ratio is too low to trigger the streaming instability in all cases. In (B, D, F), the evaporation fronts of corundum (green), forsterite (orange), albite (red), and troilite (blue) are denoted by arrows. (For interpretation of the references to colour in this figure legend, the reader is referred to the web version of this article.)

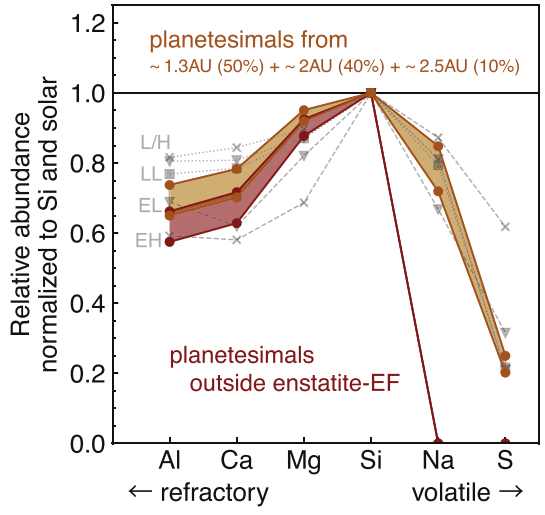

Fig. 10. Modeled abundances of Al, Ca, Mg, Na, and S normalized by Si and by the solar composition. The composition of planetesimals predicted to form outside the evaporation front (EF) of enstatite is shown in red. The initial composition does not contain Na and S because of the high disk temperature, but the volatile content is expected to increase during the later stages by accreting pebbles formed further away from the Sun. The composition of planetary body where 50% comes from planetesimals formed outside EF enstatite (1.3–1.4 AU) and 40% from Na-rich pebbles formed at 1.5–2.2 AU, and 10% from S-rich pebbles formed at 2.3–2.6 AU are shown in orange. The parameters used to create this figure is the same as those used for Fig. 2. Data for ordinary (dotted), and enstatite chondrites (dashed) are shown as well (see Fig. 1 for details). (For interpretation of the references to colour in this figure legend, the reader is referred to the web version of this article.)

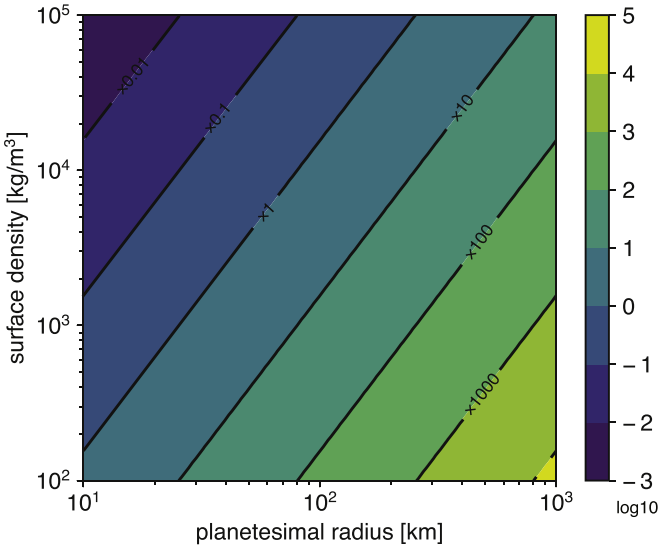

Fig. 11. The ratio of the Bondi accretion to planetesimal radii as a function of the surface density and planetesimal radius. When a Bondi accretion radius is 100 times the planetesimal radius, for example, the radius of accretion cross section is increased by 100 times from its original planetesimal size. Planetesimals can collect pebbles from a larger region as their size becomes larger and as the surface density of the surrounding gas decreases. The Bondi accretion radius is described as $GM_p/\Delta v$, where G is the gravitational constant, M_p is planetesimal mass, and Δv is difference in the orbital velocity of the gas and dust components. The parameters used to create this figure are the same as those used for Fig. 2.

volatile elements are determined by different processes; the depletion of refractory elements, including Al, Ca, and Mg, is due to the preferential loss of refractory minerals before planetesimal formation, whereas that of volatile elements arises from the disk dissipation before the accretion of volatile-bearing pebbles. Through these processes, certain chondrites can have the Na/Al ratio larger than unity, and it is not surprising to have planetesimals that are depleted in refractory elements and are enriched in volatiles at the same time.

Discrepancy between the chondrite ages and the disk evolutionary timescale would allow enough time for volatile-rich solids to be accreted onto initially dry planetesimals. The formation age of chondrites is estimated to be 1–3 Myr after CAIs (Russell et al. 1996; Kita et al. 2005), and this is later than the onset of the streaming instability triggered around the evaporation front. Considering that the evaporation front of enstatite disappears within 1 Myr of disk evolution (Ciesla 2008; Estrada et al. 2016; Miyazaki and Korenaga 2017), the streaming instability that formed silicate planetesimals has likely occurred in the first 1 Myr to produce depletion in refractory elements observed in chondrites. The younger age of chondrites may indicate a later addition or the rebuilding of planetesimals. Detailed evolution after the streaming instability is beyond the scope of this study, but such a model would be important to investigate the texture or isotopic compositions of chondrite parent bodies.

4.4. Comparison with Morbidelli et al. (2020)

The later addition of volatile-rich solids on to planetesimals created by the streaming instability has also been suggested by Morbidelli et al. (2020) to explain the major element chemistry of ordinary and enstatite chondrites. Their study also proposes that the streaming instability was triggered behind the evaporation front, but details differ considerably from this work. Instead of solving an advection-diffusion equation to model the disk transport, Morbidelli et al. (2020) assumes the existence of a local pressure maximum, which may be created at the transition from an MRI-active to inactive region. This pressure bump would accumulate dust grains and trigger the streaming instability, so they propose that, if the MRI transition was located at the evaporation front of forsterite, refractory minerals, including melilite and forsterite, would pile up at the pressure bump. When the streaming instability is triggered at the evaporation front of forsterite, refractory minerals would be sequestered in planetesimals, so the residual gas is suggested to be depleted in Al, Ca, and Mg. The compositions of ordinary and enstatite chondrites would be explained by mixing condensates from the residual gas with the unfractionated solar composition materials.

An advantage of invoking a local pressure maximum is that a higher pebble/gas ratio could be achieved than that predicted in this study. The transition from an MRI-active to inactive region, however, cannot be directly related to a pressure bump. During the early stage of protoplanetary disk evolution, an MRI-active region, which requires a sufficient level of ionization, likely appears in the hot inner region (e.g., Gammie 1996). While the inner nebula dissipates faster, it initially contains more mass than the outer region, so an outward negative pressure gradient would be maintained within the inner disk, allowing dust grains to drift inward. Given an enough time, the inner nebular would eventually be depleted, and a local pressure maximum would emerge, but even so, the disk evolution model with a spatially varying α shows that a pressure maximum would exist outside the location of the MRI-transition (Pinilla et al. 2016). Pressure gradient is affected by hysteresis, depending on the choice of initial condition. An MRI-transition may be the key to trigger the streaming instability, but a disk evolution model that tracks the pressure profile is necessary to investigate when and where the local pressure maximum would emerge within the inner disk.

Also, the residual gas may include some amount of refractory elements even if the MRI-transition creates a pressure bump at the evaporation front of forsterite. Immediately after the formation of refractory planetesimals, the residual gas is entirely depleted of refractory minerals, but it would gradually be contaminated with the surrounding gas by turbulent mixing. The surrounding gas would include some amount of refractory elements, so the abundance of refractory elements in the residual gas is expected to increase with time. The compositional evolution of protoplanetary disks is a dynamical process, so removing a certain composition does not necessarily create a corresponding residual reservoir. The assumption that the residual gas entirely lacks refractory minerals may not necessarily be the case.

A pressure bump may not exist at the location Morbidelli et al. (2020) suggested, but if a pressure bump was present somewhere inside the evaporation front of enstatite, it would accumulate highly refractory elements and create planetesimals similar to the bulk silicate Earth. The terrestrial mantle is enriched in Al and Ca compared to Si (McDonough and Sun 1995; Lyubetskaya and Korenaga, 2007), but our results show that a reservoir with an Al/Si ratio larger than unity quickly disappears in cases with $\alpha = 10^{-3}$ (Figs. 3, 7A). Because a pressure bump was not introduced in this study, highly refractory elements, including Al and Ca, are quickly lost to the Sun, which may imply the existence of a pressure bump. In future work, we plan to construct a model with a spatially varying α and investigate the effect of a pressure bump on the compositional structure.

4.5. Evolutionary path to earth formation

To explain the depletion of refractory elements observed in ordinary and enstatite chondrites, some mechanism to create nebula-wide fractionation must have operated. Considering that the protoplanetary disk was sufficiently hot to evaporate silicates only in the first million year of evolution (Cassen 2001; Chambers 2009), such mechanism has to create the depletion quickly, and the building blocks of those chondrites must also form in the depleted region. Our proposal for streaming instability occurring at the evaporation front of enstatite satisfies both of these constraints, and this suggests that planetesimals in the inner region are inevitably depleted in refractory elements. On the other hand, carbonaceous chondrites, which show no depletion in refractory elements (Wasson and Kallemeyn 1988), are likely to be created further away from the Sun. This is consistent with nucleosynthetic isotope variations observed in different chondrite groups (Burkhardt et al. 2016), which likely reflects the heliocentric distance of their source regions.

Enstatite chondrites have likely originated in the terrestrial region, but one of the challenges to forming Earth and enstatite chondrites from the same source (Javoy 1995; Javoy et al. 2010) is that they have different bulk compositions. Our model, however, suggests that planetesimals with very different Mg/Si ratios can be formed within the same isotopic reservoir. In the region around the evaporation front of enstatite, the Mg/Si ratio changes significantly within a narrow region (Fig. 3A and C), where an enrichment in Mg (Mg/Si ~1.02–1.05) is observed just inside the region where Mg is depleted. A similar trend is expected for refractory elements, including Al and Ca, if a pressure bump existed inside the evaporation front of enstatite (Section 4.4). Whereas the transport of refractory pebbles creates depletion in the region behind the enstatite evaporation front, refractories would accumulate at the pressure bump. If the pressure bump existed in the vicinity of the enstatite evaporation front, a large change in the Al/Si and Ca/Si ratios is likely around the front (Morbidelli et al. 2020). Al, Ca, and Mg are enriched in the bulk silicate Earth (Fig. 1; McDonough and Sun 1995; Lyubetskaya and Korenaga, 2007), and this suggests that planetesimals formed inside and outside the evaporation front of enstatite, respectively, may have served as the sources for Earth and enstatite chondrites. Also, they are expected to have similar isotopic compositions because the source regions for these two bodies are nearby. Our results thus suggest that similarity in isotopic compositions does not necessarily mean that their bulk compositions also resemble each other. Earth can have an isotopic composition close to enstatite chondrites and at the same time have a bulk composition close to carbonaceous chondrites.

One exception is that Earth has a heavier Si isotopic composition than enstatite chondrites. The variation of δ^{30}Si, however, correlates with the Mg/Si ratio and can be explained by the fractionation of forsterite (Dauphas et al. 2015). Therefore, the Mg/Si ratios and the δ^{30}Si values of Earth and enstatite chondrites are both consistent with the preferential loss of forsterite around the evaporation front of enstatite.

The evolutionary path to Earth formation may thus have followed the following steps: First, the radial drift of pebbles in the presence of evaporation fronts caused a depletion in refractory elements around the terrestrial region of the protoplanetary disk. In order to create a large enough depletion seen in ordinary and enstatite chondrites, the inward transport of pebbles should have been sufficiently efficient. Such a high flux of pebbles then resulted in pebble accumulation at the evaporation front of enstatite, naturally leading to the formation of planetesimals by the streaming instability. Whereas planetesimals formed outside the evaporation front remained in their original sizes and became sources for ordinary and enstatite chondrites, those formed just inside the evaporation front may have become the building blocks of Earth.

Declaration of Competing Interest

The authors declare that they have no known competing financial interests or personal relationships that could have appeared to influence the work reported in this paper.

Acknowledgments

This work was supported in part by the facilities and staff of the Yale University Faculty of Arts and Sciences High Performance Computing Center. The authors also thank Alessandro Morbidelli, John Wettlaufer, and two anonymous reviewers, whose comments were helpful to improve the accuracy of the manuscript.

Appendix A. Method details

A.1. Vertical temperature structure

Thermal and compositional structures are kept self-consistent by solving the vertical structure of the protoplanetary disk as described in Miyazaki and Korenaga (2017). Temperature at the disk surface, T_s, is calculated from the effective temperature,

$$T_s = \frac{T_e}{2^{1/4}} \tag{11}$$

and the midplane temperature T_m is calculated by integrating Eq. (3):

$$T_m = T_s + \int_0^\infty \frac{3\overline{\kappa_R}\rho_g}{16\sigma_B T^3} F_z dz \tag{12}$$

Temperature variation in the vertical direction affects the gas and dust compositions at different heights, resulting in a change in the Rosseland mean opacity. Therefore, the mass and composition of dust grains are solved at each height simultaneously with temperature using Gibbs energy minimization, and the calculated dust property is used to determine opacity. The radiative flux F_z is also calculated downwards from the surface to the midplane together with Eq. (3) using the following equation:

$$\frac{dF_z}{dz} = \frac{9}{4}\nu\rho_g\Omega_k^2 \tag{13}$$

with a boundary condition of $F_z = 0$ at the midplane ($z = 0$).

The Rosseland mean opacity is calculated at each height as a function of the dust/gas ratio, grain size, and temperature, and we use the opacity data obtained in Miyazaki and Korenaga (2017). As a first-order estimate, the opacity of silicate is used for all dust compositions in this study. The grain size distribution is assumed to follow a power law as described in Section 2.4, but the maximum grain size becomes smaller away from the midplane. Besides from the low dust density, which slows down the dust growth, disk turbulence would reset the grain size to the initial nucleation size. Turbulence would transfer gas and solid grains both upward and downward across the vertical evaporation front, so dust-composing elements would experience repeated evaporation and condensation (Miyazaki and Korenaga 2017). We thus assume a maximum grain size of 1 μm at heights below which a certain mineral evaporates and forms an evaporation front. The effect of pebbles on opacity is negligible compared to that of dust with small grain sizes because the opacity is inversely proportional to the grain size for grains larger than 1 μm (Pollack et al. 1985).

A.2. Accretionary timescale

The accretionary timescale $\tau_{d\to p}$ is closely related to the timescale of dust grain growth, τ_g. Assuming that collisions between dust grains are driven by turbulence and also that grains stick perfectly upon each collision, τ_g is expressed as (Drążkowska et al., 2016)

$$\tau_g = \frac{s}{ds/dt} = \frac{1}{\sqrt{3}\Omega_K}\frac{\Sigma_g}{\Sigma_d} \tag{14}$$

where Σ_d is the dust surface density. In regions where silicates are condensing but not ice, the dust/gas ratio is ~0.005, and τ_g is estimated to be ~100 years at 1 AU. Eq. (14) describes the dust growth rate assuming that all dust particles are of the same grain size, whereas $\tau_{d\to p}$ describes the timescale of pebble formation, where large dust grains sweep up smaller particles. The two timescales are not identical, but they both involve incremental growth through collision and are expected to fall into the same order of magnitude. Indeed, cases with $\tau^0_{d\to p}$=100 years reproduce the roughly constant profile of pebble/dust ratio in Estrada et al. (2016). We thus test 100 and 1000 years for the values of $\tau^0_{d\to p}$, the latter of which describes a case when sticking is less efficient.

A.3. The implementation of porosity

We tested different porosities for pebbles, where a higher porosity results in a larger surface area and thus enhances re-condensation onto pebbles. When pebbles are highly porous, the streaming instability may be possible even with a longer accretionary timescale or a larger pebble size. Porosity is described using the exponent q in the following equation in our model:

$$\frac{M_p}{M_d} = \frac{S_p}{S_d}\left(\frac{r_p}{r_d}\right)^q \tag{15}$$

where M denotes the total mass, S is the total surface area, and r is the grain radius of each component. Subscripts p and d indicate the pebble and dust components, respectively. Spherical pebbles correspond to $q = 1$, whereas porous pebbles could have the value as low as 0. We tested 1, 1/2, and 1/4 for the possible values of q, and the pebble/gas ratio increases around the evaporation front of enstatite as a smaller value of q is adopted. In regions away from the evaporation front, however, the effect of re-condensation is insignificant, and the pebble/gas ratio does not change much with q.

Appendix B. Planetesimal formation by gravitational instability

In order to overcome various growth barriers, we assume that planetesimals are created directly from pebbles through gravitational instabilities. The streaming instability (Youdin and Goodman 2005; Johansen et al. 2007, 2014) is considered in this paper, which concentrates pebbles into dense filaments, which can further collapse into planetesimals under self-gravity. The other potential mechanism, turbulent concentration (Cuzzi et al. 2001, 2008), is not considered here because the degree of turbulent concentration is recently suspected to be lower than initially proposed (Pan et al. 2011).

Turbulent concentration has been considered as a possible mechanism to create planetesimals especially in the inner disk because, without the re-condensation of evaporated dust grains onto pebbles, the streaming instability has been considered unlikely. The streaming instability requires a large pebble/gas ratio, but the amount of solid in the inner region is smaller than in the outer region because of the lack of icy particles. This issue may be circumvented by turbulent concentration because turbulence may locally concentrate pebble-size grains by a factor of 100 or more, resulting in gravitational instability (Cuzzi et al. 2001, 2008). Because this mechanism does not require an enhancement of the dust/gas ratio, turbulent concentration could potentially create planetesimals at anytime and any place of the protoplanetary disk.

In our model, the region where refractory elements are depleted, especially where Mg is depleted, exists only in a narrow region, and such a region moves towards the inner disk as the disk evolves (Fig. 7). If gravitational instability induced by turbulent concentration were the mechanism to create parent bodies for ordinary and enstatite chondrites, it also implies that the source regions for those chondrites are likely to be distributed throughout the disk. In such a case, the source regions for ordinary and carbonaceous chondrites have a high probability of overlapping. This, however, would not explain the nucleosynthetic isotope variations observed in different chondrite groups (Burkhardt et al. 2016). We thus suggest that, from the perspective of major element chemistry, the streaming instability is a more likely mechanism to explain the nucleosynthetic anomalies.

References

Aguichine, A., Mousis, O., Devouard, B., Ronnet, T., 2020. Rocklines as cradles for refractory solids in the protosolar nebula. Astrophys. J. 901, 97. https://doi.org/10.3847/1538-4357/abaf47.

Albarède, F., Albalat, E., Lee, C.T.A., 2014. An intrinsic volatility scale relevant to the Earth and Moon and the status of water in the Moon. Meteorit. Planet. Sci. 10, 1–10. https://doi.org/10.1111/maps.12331.

Allègre, C.J., Poirier, J.p., Humler, E., Hofmann, A.W., 1995. The chemical composition of the Earth. Earth Planet. Sci. Lett. 134, 515–526.

Armitage, P.J., 2011. Dynamics of protoplanetary disks. Annu. Rev. Astron. Astrophys. 49, 195–236. https://doi.org/10.1146/annurev-astro-081710-102521.

Bai, X.N., Stone, J.M., 2013. Local study of accretion disks with a strong vertical magnetic field: Magnetorotational instability and disk outflow. Astrophys. J. 767, 30–47. https://doi.org/10.1088/0004-637X/767/1/30.

Balbus, S.A., Hawley, J.F., 1991. A powerful local shear instability in weakly magnetized disks. I. Linear analysis. Astrophys. J. 376, 214–222.

Birnstiel, T., Dullemond, C.P., Brauer, F., 2010. Gas- and dust evolution in protoplanetary disks. Astron. Astrophys. 513, A79. https://doi.org/10.1051/0004-6361/200913731.

Brauer, F., Dullemond, P., Henning, T., 2008. Coagulation, fragmentation and radial motion of solid particles in protoplanetary disks. Astron. Astrophys. 480, 859–877. https://doi.org/10.1051/0004-6361:20077759.

Burkhardt, C., Borg, L.E., Brennecka, G.A., Shollenberger, Q.R., Dauphas, N., Kleine, T., Sauveur, S., 2016. A nucleosynthetic origin for the Earth's anomalous ^{142}Nd composition. Nature 537, 394–398. https://doi.org/10.1038/nature18956.

Cassen, P., 1996. Models for the fractionation of moderately volatile elements in the solar nebula. Meteorit. Planet. Sci. 31, 793–806.

Cassen, P., 2001. Nebular thermal evolution and the properties of primitive planetary materials. Meteorit. Planet. Sci. 36, 671–700.

Chambers, J.E., 2009. An analytic model for the evolution of a viscous, irradiated disk. Astrophys. J. 705, 1206–1214. https://doi.org/10.1088/0004-637X/705/2/1206.

Ciesla, F.J., 2008. Radial transport in the solar nebula: implications for moderately volatile element depletions in chondritic meteorites. Meteorit. Planet. Sci. 43, 639–655. https://doi.org/10.1111/j.1945-5100.2008.tb00675.x.

Ciesla, F.J., Cuzzi, J.N., 2006. The evolution of the water distribution in a viscous protoplanetary disk. Icarus 181, 178–204. https://doi.org/10.1016/j.icarus.2005.11.009.

Clayton, R.N., Mayeda, T.K., 1984. The oxygen isotope record in Murchison and other carbonaceous chondrites. Earth Planet. Sci. Lett. 67, 151–161. https://doi.org/10.1016/0012-821X(84)90110-9.

Cuzzi, J.N., Zahnle, K.J., 2004. Material enhancement in protoplanetary nebulae by particle drift through evaporation fronts. Astrophys. J. 614, 490–496. https://doi.org/10.1086/423611.

Cuzzi, J.N., Hogan, R.C., Paque, J.M., Dobrovolskis, A.R., 2001. Size-selective concentration of chndrules and other small particles in protoplanetary nebula turbulence. Astrophys. J. 546, 496–508. https://doi.org/10.1086/318233.

Cuzzi, J.N., Davis, S.S., Dobrovolskis, A.R., 2003. Blowing in the wind. II. Creation and redistribution of refractory inclusions in a turbulent protoplanetary nebula. Icarus 166, 385–402. https://doi.org/10.1016/j.icarus.2003.08.016.

Cuzzi, J.N., Hogan, R.C., Shariff, K., 2008. Toward planetesimals: dense chondrule clumps in the protoplanetary nebula. Astrophys. J. 687, 1432–1447. https://doi.org/10.1086/591239.

Dauphas, N., 2017. The isotopic nature of the Earth's accreting material through time. Nature 541, 521–524. https://doi.org/10.1038/nature20830.

Dauphas, N., Davis, A.M., Marty, B., Reisberg, L., 2004. The cosmic molybdenum-ruthenium isotope correlation. Earth Planet. Sci. Lett. 226, 465–475. https://doi.org/10.1016/j.epsl.2004.07.026.

Dauphas, N., Poitrasson, F., Burkhardt, C., Kobayashi, H., Kurosawa, K., 2015. Planetary and meteoritic Mg/Si and δ^{30}Si variations inherited from solar nebula chemistry. Earth Planet. Sci. Lett. 427, 236–248. https://doi.org/10.1016/j.epsl.2015.07.008.

Davis, S.W., Stone, J.M., Pessah, M.E., 2010. Sustained magnetorotational turbulence in local simulations of stratified disks with zero net magnetic flux. Astrophys. J. 713, 52–65. https://doi.org/10.1088/0004-637X/713/1/52.

Desch, S.J., Estrada, P.R., Kalyaan, A., Cuzzi, J.N., 2017. Formulas for radial transport in protoplanetary disks. Astrophys. J. 840, 86. https://doi.org/10.3847/1538-4357/aa6bfb.

Drążkowska, J., Alibert, Y., 2017. Planetesimal formation starts at the snow line. Astron. Astrophys. 608, A92. https://doi.org/10.1051/0004-6361/201731491.

Drążkowska, J., Alibert, Y., Moore, B., 2016. Close-in planetesimal formation by pile-up of drifting pebbles. Astron. Astrophys. 594, A105. https://doi.org/10.1051/0004-6361/201628983.

Dullemond, C.P., Dominik, C., 2005. Dust coagulation in protoplanetary disks: a rapid depletion of small grains. Astron. Astrophys. 434, 971–986. https://doi.org/10.1051/0004-6361:20042080.

Ebel, D.S., Alexander, C.M.O., 2005. Condensation from cluster-IDP enriched vapor inside the snow line: Impliactions for Mercury, astroids, and enstatite chondrites. In: 36th Lunar and Planetary Science Conference, p. 1797.

Estrada, P.R., Cuzzi, J.N., Morgan, D.A., 2016. Global modeling of nebulae with particle growth, drift, and evaporation fronts. I. Methodology and typical results. Astrophys. J. 818, 200–240. https://doi.org/10.3847/0004-637X/818/2/200.
Fedkin, A.V., Grossman, L., 2006. The fayalite content of chondritic olivine: obstacle to understanding the condensation of rocky material. In: Lauretta, D.S., McSween Jr., H.Y. (Eds.), Meteorites and the Early Solar System II. University of Arizona Press, pp. 279–294.
Gammie, C.F., 1996. Layered accretion in T Tauri disks. Astrophys. J. 457, 355–362. https://doi.org/10.1086/176735.
Grossman, L., 1972. Condensation in the primitive solar nebula. Geochim. Cosmochim. Acta 36, 597–619.
Grossman, L., Beckett, J.R., Fedkin, A.V., Simon, S.B., Ciesla, F.J., 2008. Redox conditions in the solar nebula: observational, experimental, and theoretical constraints. Rev. Mineral. Geochem. 68, 93–140. https://doi.org/10.2138/rmg.2008.68.7.
Halliday, A.N., Wood, B.J., 2015. The composition and major reservoirs of the Earth around the time of the Moon-forming giant impact. In: Schubert, G. (Ed.), Treatise on Geophysics, , Second edition9. Elsevier, pp. 11–42. https://doi.org/10.1016/B978-044452748-6.00139-5.
Hezel, D.C., Russell, S.S., Ross, A.J., Kearsley, A.T., 2008. Modal abundances of CAIs: implications for bulk chondrite element abundances and fractionations. Meteorit. Planet. Sci. 43, 1879–1894. https://doi.org/10.1111/j.1945-5100.2008.tb00649.x.
Jagoutz, E., Palme, H., Baddenhausen, H., Blum, K., Cendales, M., Dreibus, G., Spettel, B., Lorenz, V., Wanke, H., 1979. The abundances of major, minor and trace elements in the earth's mantle as derived from primitive ultramafic nodules. In: Proceedings of the 10th Lunar and Planetary Science Conference, pp. 2031–2050.
Javoy, M., 1995. The integral enstatite chondrite model of the Earth. Geophys. Res. Lett. 22, 2219–2222. https://doi.org/10.1029/95GL02015.
Javoy, M., Kaminski, E., Guyot, F., Andrault, D., Sanloup, C., Moreira, M., Labrosse, S., Jambon, A., Agrinier, P., Davaille, A., Jaupart, C., 2010. The chemical composition of the Earth: enstatite chondrite models. Earth Planet. Sci. Lett. 293, 259–268. https://doi.org/10.1016/j.epsl.2010.02.033.
Johansen, A., Lambrechts, M., 2017. Forming planets via pebble accretion. Annu. Rev. Earth Planet. Sci. 45, 359–387. https://doi.org/10.1146/annurev-earth-063016-020226.
Johansen, A., Oishi, J.S., Mac Low, M.M., Klahr, H., Henning, T., Youdin, A.N., 2007. Rapid planetesimal formation in turbulent circumstellar disks. Nature 448, 1022–1025. https://doi.org/10.1038/nature06086.
Johansen, A., Youdin, A., Mac Low, M.M., 2009. Particle clumping and planetesimal formation depend strongly on metallicity. Astrophys. J. 704, L75–L79. https://doi.org/10.1088/0004-637X/704/2/L75.
Johansen, A., Blum, J., Tanaka, H., Ormel, C., Bizzarro, M., Rickman, H., 2014. The multifaceted planetesimal formation process. In: Beuther, H., Klessen, R.S., Dullemond, C.P., Henning, T.K. (Eds.), Protostars and Planets VI. The University of Arizona Press, Tucson, AZ, pp. 547–570.
Kita, N.T., Huss, G.R., Tachibana, S., Amelin, Y., Nyquist, L.E., Hutcheon, I.D., 2005. Constraints on the origin of chondrules and CAIs from short-lived radionuclides. In: Krot Scott, A.N. (Ed.), Chondrites and the Protoplanetary Disk. Astronomical Society of the Pacific, pp. 558–587.
Kuroda, D., Hashimoto, A., 2002. The reaction of forsterite with hydrogen – its apparent and real temperature dependences. Antarctic Meteor. Res. 15, 152–164.
Lambrechts, M., Johansen, A., 2012. Rapid growth of gas-giant cores by pebble accretion. Astron. Astrophys. 544, A32. https://doi.org/10.1051/0004-6361/201219127.
Larimer, J.W., 1967. Chemical fractionations in meteorites—I. Condensation of the elements. Geochim. Cosmochim. Acta 31, 1215–1238. https://doi.org/10.1016/S0016-7037(67)80013-9.
Larimer, J.W., Bartholomay, M., 1979. The role of carbon and oxygen in cosmic gases: some applications to the chemistry and mineralogy of enstatite chondrites. Geochim. Cosmochim. Acta 43, 1455–1466. https://doi.org/10.1016/0016-7037(79)90140-6.
Lehner, S.W., Petaev, M.I., Zolotov, M.Y., Buseck, P.R., 2013. Formation of niningerite by silicate sulfidation in EH3 enstatite chondrites. Geochim. Cosmochim. Acta 101, 34–56. https://doi.org/10.1016/j.gca.2012.10.003.
Li, M., Huang, S., Petaev, M.I., Zhu, Z., Steffen, J.H., 2020. Dust condensation in evolving discs and the composition of planetary building blocks. Mon. Not. R. Astron. Soc. 495, 2543–2553. https://doi.org/10.1093/mnras/staa1149.
Lodders, K., 2003. Solar system abundances and condensation temperature of the elements. Astrophys. J. 591, 1220–1247. https://doi.org/10.1086/375492.
Lyubetskaya, T., Korenaga, J., 2007. Chemical composition of Earth's primitive mantle and its variance: 1. Method and results. J. Geophys. Res. 112, B03211. https://doi.org/10.1029/2005JB004223.
McDonough, W.F., Sun, S.s., 1995. The composition of the Earth. Chem. Geol. 120, 223–253. https://doi.org/10.1016/0012-821X(95)00123-T.
Miyazaki, Y., Korenaga, J., 2017. Effects of chemistry on vertical dust motion in early protoplanetary disks. Astrophys. J. 849, 41. https://doi.org/10.3847/1538-4357/aa8cd1.
Morbidelli, A., Libourel, G., Palme, H., Jacobson, S.A., Rubie, D.C., 2020. Subsolar Al/Si and Mg/Si ratios of non-carbonaceous chondrites reveal planetesimal formation during early condensation in the protoplanetary disk. Earth Planet. Sci. Lett. 538, 116220. https://doi.org/10.1016/j.epsl.2020.116220.
Nagahara, H., 2018. Kinetics of gas-solid reactions in the solar system and beyond. Rev. Mineral. Geochem. 84, 461–497. https://doi.org/10.1038/2051042a0.
Nelson, R.P., Gressel, O., Umurhan, O.M., 2013. Linear and non-linear evolution of the vertical shear instability in accretion discs. Mon. Not. R. Astron. Soc. 435, 2610–2632. https://doi.org/10.1093/mnras/stt1475.
Okuzumi, S., Tanaka, H., Takeuchi, T., Sakagami, M.a., 2011. Electrostatic barrier against dust growth in protoplanetary disks. I. Classifying the evolution of size distribution. Astrophys. J. 731, 95–114. https://doi.org/10.1088/0004-637X/731/2/95.
Ormel, C.W., Cuzzi, J.N., 2007. Closed-form expressions for particle relative velocities (research note). Astron. Astrophys. 466, 413–420. https://doi.org/10.1051/0004-6361:20066899.
Pan, L., Padoan, P., Scalo, J., Kritsuk, A.G., Norman, M.L., 2011. Turbulent clustering of protoplanetary dust and planetesimal formation. Astrophys. J. 740, 6. https://doi.org/10.1088/0004-637X/740/1/6.
Petaev, M.I., Wood, J.A., 1998. The condensation with partial isolation (CWPI) model of condensation in the solar nebula. Meteorit. Planet. Sci. 33, 1123–1137. https://doi.org/10.1111/j.1945-5100.1998.tb01717.x.
Pignatale, F.C., Charnoz, S., Chaussidon, M., Jacquet, E., 2018. Making the planetary material diversity during the early assembling of the Solar System. Astrophys. J. Lett. 867, L23. https://doi.org/10.3847/2041-8213/aaeb22.
Pinilla, P., Flock, M., Ovelar, M.D.J., Birnstiel, T., 2016. Can dead zones create structures like a transition disk? Astron. Astrophys. 596, A81. https://doi.org/10.1051/0004-6361/201628441.
Pollack, J.B., McKay, C.P., Christofferson, B.M., 1985. A calculation of the Rosseland mean opacity of dust grains in primordial solar system nebulae. Icarus 64, 471–492. https://doi.org/10.1016/0019-1035(85)90069-7.
Robie, R.A., Hemingway, B.S., 1995. Thermodynamic properties of minerals and related substances at 298.15 K and 1 bar pressure and at higher temperatures. In: U.S. Geological Survey Bulletin, 2131.
Russell, S.S., Srinivasan, G., Huss, G.R., Wasserburg, G.J., MacPherson, G.J., 1996. Evidence for widespread ^{26}Al in the solar nebula and constraints for nebula time scales. Science 273, 757–762. https://doi.org/10.1126/science.273.5276.757.
Scott, E.R.D., Krot, A.N., 2014. Chondrites and their components. In: Holland, H.D., Turekian, K. (Eds.), Treatise on Geochemistry, , Second edition1. Elsevier, pp. 65–137.
Shakura, N.I., Sunyaev, R.A., 1973. Black holes in binary systems. Observational appearance. Astron. Astrophys. 24, 337–355. https://doi.org/10.1086/170270.
Stewart, S.T., Leinhardt, Z.M., 2009. Velocity-dependent catastrophic disruption criteria for planetesimals. Astrophys. J. 691, L133–L137. https://doi.org/10.1088/0004-637X/691/2/L133.
Stoll, M.H.R., Kley, W., 2014. Vertical shear instability in accretion disc models with radiation transport. Astron. Astrophys. 572, A77. https://doi.org/10.1051/0004-6361/201424114.
Takigawa, A., Tachibana, S., Nagahara, H., Ozawa, K., Yokoyama, M., 2009. Anisotropic evaporation of forsterite and its implication for dust dormation conditions in circumstellar environments. Astrophys. J. 707, L97–L101. https://doi.org/10.1088/0004-637X/707/1/L97.
Vollstaedt, H., Mezger, K., Alibert, Y., 2020. Carbonaceous chondrites and the condensation of elements from the solar nebula. Astrophys. J. 897, 82. https://doi.org/10.3847/1538-4357/ab97b4.
Wasson, J.T., Kallemeyn, G.W., 1988. Compositions of chondrites. Phil. Trans. R. Soc. A 325, 535–544.
Weidenschilling, S.J., 2000. Formation of planetesimals and accretion of the terrestrial planets. Space Sci. Rev. 92, 295–310.
Windmark, F., Birnstiel, T., Ormel, C.W., Dullemond, C.P., 2012. Breaking through: the effects of a velocity distribution on barriers to dust growth. Astron. Astrophys. 544, L16. https://doi.org/10.1051/0004-6361/201220004.
Yang, C.C., Johansen, A., Carrera, D., 2017. Concentrating small particles in protoplanetary disks through the streaming instability. Astron. Astrophys. 606, A80. https://doi.org/10.1051/0004-6361/201630106.
Youdin, A.N., Goodman, J., 2005. Streaming instabilities in protoplanetary disks. Astrophys. J. 620, 459–469. https://doi.org/10.1086/426895.
Zsom, A., Ormel, C.W., Guettler, C., Blum, J., Dullemond, C.P., 2010. The outcome of protoplanetary dust growth: pebbles, boulders, or planetesimals? II. Introducing the bouncing barrier. Astron. Astrophys. 513, A57. https://doi.org/10.1051/0004-6361/200912976.